



HAL
open science

Polycomb-dependent differential chromatin compartmentalization determines gene co-regulation in Arabidopsis

Ying Huang, Sanchari Sicar, Juan S Ramirez-Prado, Deborah Manza-Mianza, Javier Antunez-Sanchez, Rim Brik-Chaouche, Natalia y Rodriguez-Granados, Jing An, Catherine Bergounioux, Magdy M Mahfouz, et al.

► **To cite this version:**

Ying Huang, Sanchari Sicar, Juan S Ramirez-Prado, Deborah Manza-Mianza, Javier Antunez-Sanchez, et al.. Polycomb-dependent differential chromatin compartmentalization determines gene co-regulation in Arabidopsis. *Genome Research*, 2021, 31 (7), pp.1-63. 10.1101/gr.273771.120 . hal-03469045

HAL Id: hal-03469045

<https://hal.science/hal-03469045v1>

Submitted on 7 Dec 2021

HAL is a multi-disciplinary open access archive for the deposit and dissemination of scientific research documents, whether they are published or not. The documents may come from teaching and research institutions in France or abroad, or from public or private research centers.

L'archive ouverte pluridisciplinaire **HAL**, est destinée au dépôt et à la diffusion de documents scientifiques de niveau recherche, publiés ou non, émanant des établissements d'enseignement et de recherche français ou étrangers, des laboratoires publics ou privés.



Distributed under a Creative Commons Attribution - NonCommercial 4.0 International License

1 **Polycomb-dependent differential chromatin compartmentalization determines**
2 **gene co-regulation in *Arabidopsis***

3
4 Ying Huang¹, Sanchari Sicar¹, Juan S. Ramirez-Prado¹, Deborah Manza-Mianza¹, Javier Antunez-Sanchez²,
5 Rim Brik-Chaouche¹, Natalia Y. Rodriguez-Granados¹, Jing An¹, Catherine Bergounioux¹, Magdy M.
6 Mahfouz³, Heribert Hirt^{1,3}, Martin Crespi¹, Lorenzo Concia^{1,4}, Fredy Barneche⁴, Simon Amiard⁵, Aline V.
7 Probst⁵, Jose Gutierrez-Marcos², Federico Ariel⁶, Cécile Raynaud¹, David Latrasse^{1*} and Moussa
8 Benhamed^{*1,7,8}

- 9
10 1- Université Paris-Saclay, CNRS, INRAE, Univ Evry, Institute of Plant Sciences Paris-Saclay (IPS2), 91405,
11 Orsay, France.
12 2- School of Life Science, University of Warwick, Coventry CV4 7AL, UK
13 3- Division of Biological and Environmental Sciences and Engineering, King Abdullah University of Science
14 and Technology, Thuwal 23955-6900, Kingdom of Saudi Arabia
15 4- Institut de Biologie de l'Ecole Normale Supérieure (IBENS), ENS, CNRS UMR8197, INSERM U1024, PSL
16 Research University, Paris, France.
17 5- GReD, Université Clermont Auvergne, CNRS, INSERM, BP 38, 63001, Clermont-Ferrand, France
18 6- Instituto de Agrobiotecnología del Litoral, CONICET, Universidad Nacional del Litoral, Colectora Ruta
19 Nacional 168 km 0, 3000, Santa Fe, Argentina
20 7- Université de Paris, Institute of Plant Sciences Paris-Saclay (IPS2), F-75006 Paris, France.
21 8- Institut Universitaire de France (IUF).

22
23 * Correspondence to: DL (david.latrasse@u-psud.fr) and MB (moussa.benhamed@u-psud.fr)

24
25 **Running title:** H3K27me3 triggers repressive loop formation

26 **Keywords:** Chromatin architecture, Chromatin loops, Polycomb, Capture Hi-C, HiChIP

27
28
29
30
31
32

33 **Abstract**

34 In animals, distant H3K27me3-marked Polycomb targets can establish physical interactions forming
35 repressive chromatin hubs. In plants, growing evidence suggests that H3K27me3 acts directly or
36 indirectly to regulate chromatin interactions, although how this histone modification modulates 3D
37 chromatin architecture remains elusive. To decipher the impact of the dynamic deposition of H3K27me3
38 on the *Arabidopsis thaliana* nuclear interactome, we combined genetics, transcriptomics and several 3D
39 epigenomic approaches. By analyzing mutants defective for histone H3K27 methylation or
40 demethylation we uncovered the crucial role of this chromatin mark in short- and previously unnoticed
41 long-range chromatin loop formation. We found that a reduction in H3K27me3 levels led to a decrease in
42 the interactions within Polycomb-associated repressive domains. Regions with lower H3K27me3 levels in
43 the H3K27 methyltransferase *clf* mutant established new interactions with regions marked with H3K9ac
44 –a histone modification associated with active transcription–, indicating that a reduction in H3K27me3
45 levels induces a global reconfiguration of chromatin architecture. Altogether, our results reveal that the
46 3D genome organization is tightly linked to reversible histone modifications that govern chromatin
47 interactions. Consequently, nuclear organization dynamics shapes the transcriptional reprogramming
48 during plant development and places H3K27me3 as a key feature in the co-regulation of distant genes.

49

50

51

52

53

54

55

56

57

58 **Introduction**

59 Gene expression regulation underlying eukaryotic cell differentiation depends largely on covalent
60 modifications of nuclear chromatin, including histone modifications (Ahmad et al. 2010). It has been
61 shown that histone modifications alter chromatin condensation, which ultimately affects global genome
62 topology in the nucleus, as well as the local chromatin 3D conformation, thereby modulating the
63 accessibility of specific loci to the transcriptional machinery (Rodriguez-Granados et al. 2016; Huang et
64 al. 2020). In the last few years, the concept of genetic information encoded in a linear sequence of
65 nucleotides associated with histones has evolved into a more comprehensive viewpoint considering the
66 dynamic 3D architecture of the cell nucleus (Misteli 2007). From this perspective, structural elements
67 such as *loops*, *domains*, *territories* and *factories* emerge as crucial functional features controlling the
68 physical interaction between promoters and distant regulatory elements (Sutherland and Bickmore
69 2009), as well as the spatial organization of transcriptional hubs. Consequently, nuclear organization
70 dynamics appear as an integrator of developmental and environmental signals (Huang et al. 2020).

71 The advent of innovative methods to study genome-wide 3D spatial chromatin organization from a
72 molecular perspective, such as Hi-C, HiChIP, and ChIA-PET, has allowed to uncover both small- and large-
73 scale genome architecture in various cell types of metazoan organisms, notably in mammals (Mishra and
74 Hawkins 2017; Fullwood et al. 2009; Mumbach et al. 2016; Mifsud et al. 2015). This has revealed the
75 existence of megabase-long chromatin compartments comprising either active (A compartment) or
76 inactive chromatin (B compartment) (Dong et al. 2017b; Rowley et al. 2017; Fortin and Hansen 2015).
77 Furthermore, it also allowed the identification of topologically associated domains (TADs) as
78 fundamental units of 3D genome organization. TADs are large self-interacting genomic regions
79 (Gonzalez-Sandoval and Gasser 2016; Rocha et al. 2015; Dixon et al. 2016, 2012), which encompass
80 genes displaying similar expression dynamics, suggesting that physical association is functionally relevant
81 for the control of transcriptional activity (Dekker and Heard 2015). Higher-resolution studies have shown

82 that TADs can be further-subdivided into compartmental domains which formation appears to be
83 governed by transcription (Rao et al. 2017; Rowley et al. 2017).

84 Even though plant and metazoan nuclei share certain commonalities, they also display radical differences
85 (Feng et al. 2014; Grob et al. 2014; Dong et al. 2017a; Mascher et al. 2017; Rodriguez-Granados et al.
86 2016; Huang et al. 2020). Notably, plants lack genes encoding CTCF transcription factors, which have
87 been pointed in animals as key players in the establishment of TADs and chromatin loops (de Wit et al.
88 2015; Guo et al. 2015). Pioneer Hi-C analyses revealed the absence of TAD-like structures in *Arabidopsis*
89 *thaliana* (Wang et al. 2015; Feng et al. 2014; Grob et al. 2014), a phenomenon that has been attributed
90 to the small size of its compact genome, which exhibits relatively homogenous transcriptional rates and
91 a low density of noncoding regions (Rowley and Corces 2016; Rowley et al. 2017). Recent studies in
92 plants with large and complex genomes have revealed the existence of TAD-like domains (Liu et al. 2017;
93 Wang et al. 2018; Dong et al. 2018; Concia et al. 2020; Dong et al. 2017a). However, unlike their animal
94 counterparts, these TAD-like structures mainly correspond to large heterochromatic compartments,
95 suggesting that they should rather be referred to as ICONS (Intergenic CONDensed Spacers), as they are
96 not functionally equivalent to TADs (Huang et al. 2020 ; Concia et al. 2020).

97 The existence of a large repertoire of histone modifications and variants with distinct physical properties
98 and associated to diverse chromatin states (e.g. constitutive heterochromatin, facultative
99 heterochromatin, euchromatin), allows the establishment of a highly precise cell-specific transcriptional
100 landscape in response to environmental and developmental stimuli (Kouzarides 2007; Eichten et al.
101 2014). The numerous changing environmental signals perceived by the cell require a pertinent response,
102 which must be accurately modulated with time (Gambino and Pantaleo 2017). Thus, reversible and
103 dynamic histone modifications permit the induction and repression of the appropriate subsets of genes
104 under certain conditions (Pfluger and Wagner 2007). In agreement, protein complexes and enzymes with
105 opposite activity upon histone covalent modifications continuously shape the chromatin environment of

106 target genes. Thus, the so-called *writers* govern the deposition of a specific covalent histone
107 modification, while *erasers* participate in their removal (Mach 2018). A third group of proteins called
108 *readers*, recognizes specific histone modifications and induces downstream processes through diverse
109 mechanisms, including chromatin compaction, remodeling, the recruitment of secondary chromatin
110 modifiers, Transcription Factors (TF) and the DNA damage repair machinery, among others (Yun et al.
111 2011).

112 The tri-methylation of the lysine 27 of histone H3 (H3K27me3) is a repressive covalent histone
113 modification resulting from the activity of Polycomb Repressive Complexes (PRCs), formed by the
114 combination of multiple Polycomb group (PcG) proteins (Grossniklaus and Paro 2014). In both animals
115 and plants, PRCs are classified into PRC1 and PRC2, in which PRC2 deposits H3K27me3 on its targets,
116 while PRC1 recognizes these histone modifications and stabilizes PRC2-mediated repression. There are
117 three SET-domain proteins with H3K27me3 methyltransferase activity in *Arabidopsis thaliana*: SWINGER
118 (SWN), CURLY LEAF (CLF) and MEDEA (MEA) (Mozgova et al. 2015). The PcGs activity in this plant model
119 is counteracted by four Jumonji (JMJ)-type proteins, which perform the active demethylation of
120 H3K27me3 and determine spatial boundaries for this histone modification, restricting its spreading and
121 the consequent formation of repressive chromatin domains (Yan et al. 2018). Among them, REF6
122 (RELATIVE OF EARLY FLOWERING 6) has been reported to promote flowering through the activation of
123 the flower integrators *FT* (*FLOWERING LOCUS T*) and *SOC1* (*SUPPRESSOR OF CO OVEREXPRESSION 1*) (Hou
124 et al. 2014; Noh et al. 2004). Moreover, the *ref6* mutation partially complements the developmental
125 phenotype and the decreased fertility caused by the *clf* mutation (Lu et al. 2011). Consistently, the *REF6*
126 over-expressing plants share several of the developmental phenotypes of *clf*, highlighting the
127 antagonistic function between this protein and the PRC2 complex (Lu et al. 2011).

128 Growing evidence indicates that H3K27me3 plays an important role in the spatial organization of
129 chromatin in eukaryotes, a phenomenon that has been associated with its repressive role in

130 transcription. For instance, it has been shown in animals that Polycomb targets marked with H3K27me3
131 can establish interactions between them, forming repressive chromatin hubs dependent on PRCs and
132 insulator proteins (Lanzuolo et al. 2007; Cheutin and Cavalli 2014). PRCs have also been shown to
133 regulate the maintenance of pluripotency in mammalian embryonic stem cells through the organization
134 of interaction networks (Schoenfelder et al. 2015), and H3K27me3 levels have been associated with the
135 *Drosophila's* genome subdivision into TADs (El-Sharnouby et al. 2017 ; Boettiger et al. 2016; Eskeland et
136 al. 2010; Francis et al. 2004; Joshi et al. 2015; Kundu et al. 2017; Williamson et al. 2012; McLaughlin et al.
137 2019). In plants, several studies suggested that this covalent histone modification is a key contributor to
138 chromatin topology. A Hi-C approach served to propose that the local interaction of H3K27me3 domains
139 is reduced in the *Arabidopsis clf/swn* double mutant background (Feng et al. 2014). Besides, it has been
140 shown that H3K27me3 is enriched at long-distance interacting loci across the *Arabidopsis* genome (Liu et
141 al. 2016a). Furthermore, in a previous study, we showed that the *Drosophila* HETEROCHROMATIN
142 PROTEIN1 (HP1) homolog in *Arabidopsis* LIKE-HP1 (LHP1) participates in the 3D-conformation of the
143 *Arabidopsis* genome (Veluchamy et al. 2016), and that its genome-wide distribution perfectly matches
144 that of H3K27me3. LHP1 is considered a component of the plant PRC1 complex, given its capacity to
145 recognize H3K27me3 through its chromodomain (Gaudin et al. 2001; Turck et al. 2007; Zhang et al.
146 2007). Therefore, H3K27me3 may directly or indirectly participate in the regulation of the dynamic
147 interactivity of Polycomb target genes. However, several aspects of the molecular function of H3K27me3
148 in 3D chromatin architecture determination remain unclear. In order to gain a deeper understanding of
149 the molecular role of H3K27me3, we combined cutting-edge technologies applied to the characterization
150 of 3D chromatin conformation.

151

152 **Results**

153 ***Arabidopsis* chromatin organization displays a strong compartmentalization**

154 The first Hi-C analyses performed in *Arabidopsis* nuclei revealed that TADs, which are widely distributed
155 among metazoans and plants, are hardly found (Liu et al. 2016a). Long-range chromatin interactions are
156 rare in this organism and correspond almost exclusively to heterochromatic regions such as
157 centromeres. A notable exception of this phenomenon is the KNOT, which brings together
158 heterochromatic islands within euchromatin (Grob et al. 2014).

159 In order to determine the extent to which chromatin compartmentalization is a characteristic feature of
160 the *Arabidopsis* genome, we performed immuno-detection of H3K27me3 and H3K9ac, two histone post-
161 translational modifications associated to gene repression and activation, respectively. The immuno-
162 staining performed on somatic nuclei during interphase revealed a heterogeneous distribution of these
163 covalent histone modifications, suggesting that distinct euchromatin and facultative heterochromatin
164 compartments exist in *Arabidopsis* (Fig. 1A and Supplemental Fig. S1). Moreover, by measuring the
165 H3K9ac and H3K27me3 signal distribution along a virtual axis arbitrarily defined in an immuno-stained
166 nucleus, we observed that the corresponding peaks are anti-correlated (Fig. 1B). Given the proximity
167 between H3K9ac and H3K27me3 marked genes along the chromosome and the resolution of the
168 confocal microscope that is about 0.5 μ m, this result suggest that actively transcribed and repressed
169 genes occupy distinct compartments within the cell nucleus. To gain a deeper understanding of the
170 compartmental organization of active and silent chromatin, we conducted HiChIP, a sensitive method for
171 the efficient analysis of protein-centric chromosome conformation (Fig. 1C, 1D and Supplemental Fig. S2)
172 (Mumbach et al. 2016). H3K27me3- and H3K9ac- HiChIPs were performed in 14-day-old wild-type (WT)
173 shoots. A minimum of 159 million of read pairs were produced for each sample, and 116 million uniquely
174 mapped read pairs were generated (Supplemental Table S1), with a high reproducibility between
175 replicates (Supplemental Fig. S3). In parallel, ChIP-seq was performed for the same histone
176 modifications. In contrast to traditional Hi-C (Fig. 1C and 1D, left panels), the HiChIP approach allows
177 revealing interactions associated with each specific histone modification (Fig. 1C and 1D, right panels).

178 Both short- and long-range interactions from few kilo-bases to several mega-bases were detected at the
179 site of the respective histone modifications (Supplemental Fig. S4 and Supplemental Table S2, S3, S4 and
180 S5). By overlapping both H3K9ac and H3K27me3 HiChIP signals, our data suggested that genes
181 associated to the same histone modification interact with each other to form contact domains and fold
182 the genome locally to allow the spatial segregation of transcriptionally active and silent chromatin (Fig.
183 1E).

184

185 **Shoot and root nuclei display distinct 3D chromatin architecture**

186 The 3D configuration of the nuclear genome is non-random and correlates with cell type-specific
187 transcriptomes; however, the mechanisms implicated in the establishment of this configuration are
188 poorly understood in plants. It has been recently shown that biosynthetic non-homologous gene clusters
189 are embedded in local 3D configurations that segregate cluster regions from the surrounding
190 chromosome environment. Based on Hi-C and H3K27me3 distribution in *Arabidopsis*, it has been
191 proposed that genome topology differs between shoots and roots (Nützmänn et al. 2020). In order to
192 further decipher the relationship between H3K27me3 and 3D chromatin conformation, we performed
193 H3K27me3- HiChIP and ChIP-seq in shoots and roots. The high-resolution interaction matrix obtained by
194 HiChIP revealed the widespread presence of interactions between genomic bins including H3K27me3-
195 enriched genes from both tissues (Supplemental Fig. S5 and S6). A differential analysis using HOMER
196 comparing shoots and roots served to identify the most informative loops associated with H3K27me3
197 (Fig. 2A), which allowed us to focus on the top shoot-specific repressive loops (SSRLs) in downstream
198 analyses (Supplemental Table S6). We found a positive correlation between H3K27me3 levels and the
199 strength of the detected interactions when SSRLs were visualized at different scales (Fig. 2B and 2C). To
200 further support our observations, we quantified the level of this histone modification in shoots and roots
201 on genes associated to SSRLs, and observed that 47% of those genes are hypermethylated in shoot

202 compared to root, confirming that this repressive histone modification is associated with chromatin loop
203 formation and/or stability (Fig. 2D and Supplemental Table S7).

204 We then wondered whether gene pairs connected in SSRLs show similar changes in expression levels
205 between shoots and roots. Using publicly available gene expression data (Liu et al. 2016b), we plotted
206 the top SSRL gene pairs using the \log_2 (fold-change shoot/root) of the first gene as the predictor and the
207 \log_2 (fold-change shoot/root) of the second gene as the response (Fig. 2E, Supplemental Fig. S7 and
208 Supplemental Table S8). This analysis revealed a significant correlation between H3K27me3 SSRL-
209 associated loci and genes repressed in shoots (Fig. 2E). These data indicate that genes displaying specific
210 physical contacts, and associated with H3K27me3, exhibit similar transcriptional behavior and are likely
211 part of common Polycomb-repressive compartments (Fig. 2E).

212 It has been extensively shown that H3K27me3 works as a repressive covalent histone modification
213 participating in the regulation of multiple developmental genes in plants (Cheng et al. 2020). Then, to
214 better understand the impact of H3K27me3-dependent chromatin architecture on plant development,
215 we performed an analysis of Gene Ontology (GO) terms enriched among loci grouped in SSRLs with a
216 lower expression in shoots than in roots. We found a significant enrichment in GO categories related to
217 root development and cell identity (Fig. 2F), hinting at a comprehensive epigenetic reprogramming of
218 developmental pathways in different organs. Reciprocally, we also explored the root specific repressive
219 loops (RSRLs) and their impact on developmental outputs (Fig. 2G and Supplemental Table S9). In
220 agreement with our observations for SSRLs, genes associated in RSRLs displayed higher H3K27me3 levels
221 in roots than in shoots and lower expression levels in roots compared to shoots (p-value = $3.2E-55$) (Fig.
222 2G-K, Supplemental Fig. S7, Supplemental Table S10 and S11). In addition, the GO analysis of genes
223 grouped in RSRLs, which are down regulated in roots, showed enrichment in categories related to shoot
224 development and photosynthesis (Fig. 2L), in agreement to the non-photosynthetic nature of root
225 tissues. These observations suggest a role of H3K27me3-dependent genome topology in coordinating the

226 transcriptional activity underlying developmental programs.

227 One limitation of HiChIP when using antibodies directed against a particular histone modification, is that
228 the detection of chromatin contact relies on the presence of this given histone modification at the site of
229 interaction. Thus, the observed reduction of the strength of some interactions could merely reflect
230 H3K27me3 depletion at loci of interest. To rule out this possibility, we performed capture-Hi-C (C-Hi-C).
231 This approach combines Hi-C with the hybridization-based capture of targeted genomic regions
232 (Supplemental Fig. S8). To this end, we generated a biotinylated RNA bait library specifically targeting
233 4,650 regions that accumulate H3K27me3 and included a subset of loci differentially methylated
234 between shoots and roots (Supplemental Fig. S9). The comparison of both Hi-C and C-Hi-C matrixes
235 allowed us to identify a significant enrichment of chromatin contacts over our target sequences (Fig. 3A)
236 and to obtain a high-resolution map of interactions between captured regions, as well as between
237 captured and non-captured regions (Fig. 3B). A differential analysis using HOMER resulted in the
238 identification of 7,676 shoot-specific loops (SSLs), of which 277 overlapped with the SSRLs previously
239 identified by HiChIP. These data suggest that the deposition of H3K27me3 participates in the
240 establishment of tissue-specific chromatin loops (Fig. 3C-E and Supplemental Table S12, S13 and S8).
241 Focusing on these SSLs identified by both methods, we found that 67% of the genes grouped in SSLs
242 were found to be specifically repressed in shoots compared to roots (Fig. 3F). This proportion is
243 significantly higher than the one expected by chance (p -value = $1.61E-144$) (Supplemental Fig. S10). On
244 the other hand, we found through the same approach 6737 root specific loops (RSLs), among which 231
245 were also found on the previously generated H3K27me3-HiChIP data analysis and defined RSRLs (Fig. 3G,
246 3H and 3I and Supplemental Table S13, S14). 54% of the genes grouped in RSLs were specifically
247 repressed in roots compared to shoots, a proportion significantly higher than the one expected by
248 chance (p -value = $2.71E-68$) (Fig. 3J and Supplemental Fig. S10). We also observed that 24% and 35% of
249 the genes respectively grouped in SSLs and RSLs displayed an unexpected behavior, what could be

250 explained by the fact that both shoots and roots correspond to complex samples of a mixture of various
251 cell types. Altogether, our C-Hi-C data further supported that the H3K27me3 levels mediate the
252 establishment and/or stability of repressive domains bringing together several genes in *Arabidopsis* and
253 that Polycomb-related repressive compartments could play an important role in the transcriptional
254 reprogramming underlying plant cell fate and organ development.

255

256 **Ectopic deposition of H3K27me3 leads to occurrence of novel chromatin repressive loops**

257 To decipher the impact of H3K27me3 levels on chromatin loop dynamics, we used the loss-of-function
258 *ref6-5* mutant, defective for a histone demethylase and displaying ectopic accumulation of H3K27me3 at
259 thousands of loci (Antunez-Sanchez et al. 2020; Lu et al. 2011; Yan et al. 2018) (Fig. 4A). Thus, in order to
260 assess if ectopic H3K27me3 deposition could lead to the formation of new repressive compartments, we
261 performed a C-Hi-C experiment comparing *ref6-5* and WT shoots (Fig. 4B-D and Supplemental Fig. S11). A
262 HOMER differential analysis identified the top *ref6-5*-specific repressive loops (reSLs) ranked according to
263 the log fold-change and Z score (Fig. 4B and Supplemental Table S15). We observed that a large
264 proportion of genes involved in reSLs displayed a significant increase in H3K27me3 levels in *ref6-5*
265 compared to WT (p-value = 4.62E-76) (Fig. 4C-E, Supplemental Fig. S12 and Supplemental Table S16). To
266 confirm this, we assessed the proportion of *ref6-5* hyper-methylated genes associated to repressive
267 loops and found that 40% were associated with reSLs (Fig. 4C-D and Fig. 4E). These data suggest that a
268 gain in H3K27me3 triggers the establishment of novel chromatin interactions (Fig. 4D). Using publicly
269 available transcriptomic data (Antunez-Sanchez et al. 2020) we assessed whether gene pairs connected
270 through reSLs showed similar transcriptional shifts between *ref6-5* and WT. We found a significant
271 enrichment of co-repressed reSL-paired genes loci among the 546 plotted couples (p-value = 4E-10) (Fig.
272 4F, Supplemental Fig. S12 and Supplemental Table S17). This result indicates that genes displaying
273 specific physical contact in *ref6-5* are globally repressed, likely linked to the ectopic accumulation

274 H3K27me3 and the formation of repressive chromatin loops.

275

276 **Reduction of H3K27me3 level induces a reconfiguration of chromatin architecture**

277 Considering that the ectopic deposition of H3K27me3 induces the formation of novel chromatin
278 repressive loops, we decided to assess the impact of a reduction in H3K27me3 deposition on the
279 interaction profile within Polycomb-related repressive domains. To this end, we used *clf-29*, a Polycomb
280 Repressive Complex 2 (PRC2) histone methyltransferase mutant that displays a strong reduction on
281 H3K27me3 levels at thousands of loci (Veluchamy et al. 2016) (Fig. 4A). C-Hi-C and a differential analysis
282 comparing *clf-29* and WT shoots identified the top *clf* Specific Disrupted Loops (cSDLs) ranked according
283 to the log fold-change and Z score (Fig. 5A, 5B, Supplemental Fig. S13 and Supplemental Table S18). We
284 observed that 33% of genes involved in cSDLs displayed a significant decrease in H3K27me3 levels in the
285 *clf-29* mutant compared to WT (p-value = 9.72E-52) (Fig. 5C, 5D, Supplemental Table S19). To confirm
286 this observation, we assessed the proportion of *clf* hypo-methylated genes associated to cSDLs and
287 found that 40% of the *clf* hypo-methylated genes are associated to a cSDL, suggesting that the loss of
288 H3K27me3 induced a destabilization of repressive loops in the *clf-29* (Fig. 5E). To uncover the impact of
289 chromatin architecture reorganization on transcriptional reprogramming, we analyzed the expression of
290 gene pairs normally brought together into spatial proximity in WT shoots, which are no longer clustered
291 in the *clf-29*. We observed a significant enrichment in transcriptionally activated genes (p-value = 4.336E-
292 7) (Fig. 5G, Supplemental Fig. S14 and Supplemental Table S20), indicating that genes involved in loops
293 lost in the *clf-29* mutant tend to be upregulated. Altogether, our results suggest that a *clf*-dependent
294 decrease in H3K27me3 leads to a re-configuration of chromatin architecture and the destabilization of
295 H3K27me3-mediated repressive loops (Fig. 5B and 5F). This phenomenon can be associated to the
296 transcriptional de-repression of hundreds of genes in PRC2-related mutants.

297 To better understand the association between genome topology reconfiguration, H3K27me3 deposition

298 and gene expression, we compared epigenomic and transcriptional features found in *clf-29* and WT, and
299 integrated these datasets with chromatin interaction positioning (Supplemental Table S21). Our analysis
300 revealed that interactions occur more frequently between genes with concordant transcriptional status,
301 independently of whether they are up- or down-regulated in *clf-29* compared to the WT (Fig. 5G and 5H).
302 Moreover, a similar trend was observed for the epigenomic profile, since genes with concordant
303 H3K27me3 levels are more prone to interact in common hubs (Fig. 5G and 5H). A higher frequency in the
304 interaction among hypomethylated genes in *clf-29* suggested a gain of novel interactions. Considering
305 that *clf*-hypomethylated genes exhibited a global transcriptional activation, we assessed in WT shoots
306 the distribution of the H3K9ac histone modification, characteristic of active loci. Then we mapped the
307 gained interactions determined by C-Hi-C in *clf-29* throughout the genome, together with the
308 distribution of the H3K9ac histone modification in the WT. We observed that regions losing H3K27me3 in
309 *clf-29* tend to establish novel interactions with regions marked with the active histone modification
310 H3K9ac (Fig. 5I and 5J, Supplemental Fig. S15 and S16, Supplemental Table S22, S23 and S24). This
311 suggests that a reduction in H3K27me3 levels induces a global reconfiguration of chromatin architecture
312 (Fig. 5J and 5K), allowing genes that lost their repressive covalent histone modification to integrate
313 transcriptionally active hubs. Altogether, our results demonstrate that the 3D genome organization is
314 tightly linked to histone modifications that dynamically modulate the determination of chromatin
315 domains associated with gene co-regulation, thereby allowing the progression of plant developmental
316 programs. Collectively, our data supports the view that H3K27me3 acts as a key regulator of global and
317 local facultative heterochromatin topology in plants.

318

319 **Discussion**

320 The first analyses of the 3D genome organization of *Arabidopsis* revealed the absence of TAD structures
321 and the existence of an “A/B” type compartmentalization at a local level, in domains of a few tens of kb

322 (Lieberman-Aiden et al. 2009; Grob et al. 2014). Constitutive heterochromatin, which contains mainly
323 transposable element marked by specific histone modifications such as H3K9me2 and H3K27me1, is one
324 of the major factors directing this compartmentalization. However, the contribution of facultative
325 heterochromatin to higher-order nuclear topology in plants is not clearly stated. In the current study,
326 through the integration of immuno-staining experiments and confocal microscopy, we provide evidence
327 that H3K9ac-rich (euchromatin) and H3K27me3-rich (facultative heterochromatin) regions are spatially
328 segregated, confirming that actively transcribed and repressed genes occupy distinct region in the
329 nucleus. This result is consistent with previous ChIP-based studies in *Arabidopsis*, which have shown that
330 the distribution of facultative heterochromatic histone modifications such as H3K27me3 on the linear
331 genome is anti-correlated to euchromatic histone modifications (Ha et al. 2011).

332 Hi-C data is useful for the depiction of the genome-wide 3D organization of chromatin in the nucleus;
333 however, to understand which proteins or covalent histone modifications have a role in structuring this
334 organization, it is necessary to integrate it with external datasets (e.g. ChIP-seq) allowing only correlative
335 analyses. To circumvent this limitation and to address whether and how genomic regions associated to
336 histones bearing a specific covalent modification interact through long-range chromatin looping in a
337 genome-wide and unbiased manner, we performed HiChIP experiments, confirming that
338 transcriptionally active and inactive genes localize in different nuclear compartments. In addition, we
339 also observed both long- and short-range interactions –ranging from a few kilo bases several mega bases
340 –enriched at the site of either H3K27me3 or H3K9ac, highlighting the role of these histone modifications
341 in 3D chromatin architecture. In plants, it has been previously hypothesized that H3K27me3 contributes
342 to the establishment of chromatin loops, as this histone modification has been detected in interacting
343 genomic regions (Liu et al. 2016a); however, in the current study we have taken advantage of the specific
344 capture of H3K27me3-labeled chromatin loops to provide evidence of the role of this covalent histone
345 modification in the spatial organization of chromatin. A similar approach has been used in maize to

346 identify *cis*-regulatory elements, revealing that H3K27me3 is potentially implicated in mediating
347 chromatin loops between regulatory elements and their target genes, in a process associated to gene
348 repression (Ricci et al. 2019).

349

350 **Chromatin architecture and development**

351 In the last few years, we have witnessed a significant increase in studies addressing the role of 3D
352 genome organization in the regulation of developmental processes as well as in response to
353 environmental cues. Hence, it is currently known that chromatin topology is highly dynamic during
354 animal developmental phase transitions, including gametogenesis, embryo development and cell
355 differentiation. The recent development of single-cell and low-input Hi-C approaches has permitted the
356 characterization of the embryo along different developmental stages, as well as different cell lines during
357 differentiation and lineage commitment. This has allowed to identify commonalities and particularities of
358 each cell type and to associate them to specific phenotypes (Zheng and Xie 2019). These single-cell
359 techniques have seldom been applied in plants, mainly due to the technical limitations that this imposes
360 (Huang et al. 2020); however, some studies have started characterizing the chromatin topology of
361 specific plant cell types, showing that as in animals, gamete, zygote and differentiated cells present
362 striking differences in their nuclear 3D chromatin configuration. By integrating single-cell 3C and Hi-C
363 approaches, Zhou and collaborators analyzed the 3D genomes of rice sperm, egg, unicellular zygote and
364 mesophyll cells, finding that rice nuclei present spatially organized chromatin territories associated to
365 different histone modifications and gene expression levels, providing evidence of the contribution of the
366 spatial organization of chromatin to the co-regulation of gene expression (Zhou et al. 2019).

367 The relevance of chromatin organization in the developmental context can be evidenced in the variety of
368 diseases and developmental problems that have been associated to abnormalities in chromatin
369 organization in various organisms. For instance, cardiac diseases, cancer and developmental disorders

370 have been attributed to mutations in genes encoding CTCFs and cohesion proteins (Rosa-Garrido et al.
371 2017; Kaiser and Semple 2017; Lupiáñez et al. 2015, 2016). Furthermore, the disruption of TAD
372 boundaries has been shown to have developmental effects as a consequence of *enhancer hijacking*, or
373 the abnormal interaction between an enhancer and a promoter. Several examples of this phenomenon
374 have been reported in the literature (Zheng and Xie 2019; Kaiser and Semple 2017; Lupiáñez et al. 2016),
375 highlighting the crucial role of chromatin organization on cell homeostasis and animal development.
376 However, studies demonstrating the developmental consequences of chromatin disorganization in
377 plants remain scarce. It has been recently shown that loss of CROWDED NUCLEI (CRWN) proteins, which
378 are candidate nuclear lamina proteins in *Arabidopsis*, leads to a general reduction on chromatin
379 organization and an associated reprogramming of the transcriptome (Choi et al. 2019; Hu et al. 2019).
380 Furthermore, the loss of these proteins has been reported to induce dwarfism and a spontaneous cell
381 death phenotype, which have been attributed to the constitutive induction of the salicylic acid-
382 dependent pathway of immunity (Hu et al. 2019). These results suggest that as in animals, 3D chromatin
383 organization plays a key role in the regulation of plant development and homeostasis. Furthermore,
384 these results suggest that several of the pleiotropic phenotypes observed in plants defective in the
385 epigenomic machinery may result from distortions in chromatin architecture and their impact on gene
386 expression; however, this needs to be experimentally assessed.

387 In the current study we provide evidence for the existence of distinctive chromatin architecture between
388 root and shoot cells, as evidenced by the presence of shoot- and root-specific repressive loops, mediated
389 by H3K27me3. This represents valuable evidence for the understanding of how chromatin modifications
390 contribute to chromatin topology and, consequently, to organ identity in plants. Our data shows that
391 genes involved in SSRLs and RSRLs are associated with biological functions specific to the studied organs,
392 supporting the view that chromatin loops contribute to the developmental differentiation of specific
393 cells types in plants (Fig. 6).

394 **Polycomb-repressed chromatin is critical for 3D nuclear organization in plants**

395 Traditionally, Polycomb complexes have been associated to the repression of developmental genes,
396 including the well described *Hox* genes (Bantignies et al. 2011; Kassis et al. 2017). However, the
397 introduction of 3D epigenomic techniques has allowed to depict some of the molecular mechanisms by
398 which these complexes regulate development, including the modulation of chromatin architecture
399 (Pachano et al. 2019; Illingworth 2019). For instance, a recent study unveiled that H3K27me3 is a
400 fundamental player in the chromatin reorganization occurring during oocyte development in mice (Du et
401 al. 2020). Polycomb-Associated Domains (PADs) are self-interacting, cohesion-independent
402 compartments enriched in H3K27me3 that are gradually established on the maternal genome until a
403 late-stage before disappearing upon meiotic resumption. Hi-C analyses of mutants defective on PRC2
404 and PRC1 subunits revealed that PAD establishment is highly dependent on these complexes and
405 H3K27me3 (Du et al. 2020). Most of the studies on the 3D organization of PcG-bound chromatin in
406 mammals have been performed in embryonic stem cells (ESCs), and have illustrated that Polycomb
407 proteins and their associated histone modifications accumulate in ESCs in discrete foci that have been
408 named *PcG bodies* (Bantignies et al. 2011; Pachano et al. 2019). Mutations in subunits of both PRC2 and
409 PRC1 have been shown to lead to the dispersion of these structures (Hernández-Muñoz et al. 2005),
410 suggesting significant changes in chromatin architecture in these mutants. The molecular mechanisms
411 connecting H3K27me3 deposition, loop formation and gene expression have been dissected into detail in
412 *Drosophila*. This study showed (i) that H3K27me3 deposition is critical for loop formation and (ii) that
413 chromatin looping contributes to gene repression, although it is not strictly required (Ogiyama et al.
414 2018). These results are coherent with our previous characterization of the *Arabidopsis lhp1* mutant,
415 deficient in a PRC1 subunit, where a vast proportion of genomic interactions are lost (Veluchamy et al.
416 2016). The loss of these interactions is associated, to a large extent, to a significant reduction on
417 H3K27me3 levels on interacting partners, suggesting that both LHP1 and H3K27me3 are involved in loop

418 formation in this organism. Since LHP1 is an H3K27me3 reader, it is considered to act, at least partially,
419 downstream of H3K27me3 methyltransferases (Berry et al. 2017). Hence, if LHP1 activity depends on
420 H3K27me3 levels, altering the latter through mutations on *CLF* or *REF6* should have an impact on
421 chromatin looping. In agreement, in the current study we found that increasing H3K27me3 levels leads
422 to the formation of new chromatin repressive loops, while reducing them has the inverse effect.
423 Altogether, these results indicate that, similar to animals, PRCs and H3K27me3 play a fundamental role
424 in the shaping of regulatory chromatin interactions and overall, chromatin conformation in the three-
425 dimensional space, a phenomenon that is associated with developmental processes and, most likely, cell
426 identity. However, the respective importance of H3K27me3 deposition and H3K27me3-mediated
427 chromatin looping for efficient gene repression will require further investigation.

428 We found that some of the regions that lose H3K27me3 in the *clf* mutant tend to establish interactions
429 with transcribed regions marked with H3K9ac. This may indicate that one of the mechanisms by which
430 H3K27me3 contributes to gene repression is through the preclusion of these interactions. In addition, in
431 animals, there is recent evidence indicating that histone hyperacetylation also contributes to nuclear
432 organization, as it induces the formation of long-range chromatin interactions and nuclear sub-
433 compartments (Rosencrance et al. 2020). This shows that the dynamic chromatin topology in the nuclear
434 space results from the delicate balance of a plethora of elements, including various histone
435 modifications, which recruit the nuclear machinery for its spatial organization. It has been proposed that
436 nuclear proteins can pull the genome into new positions like in the game "cat's cradle", where the shape
437 of a string is successively changed by opening up new sites for finger placement (Melé and Rinn 2016).
438 Future research is likely to provide exciting new insights into the mechanisms involving histone
439 modifications and associated molecules in the dynamic configuration of the plant genome.

440 In summary, our results demonstrate the 3D organization of the genome is tightly linked to histone
441 modifications that trigger the formation of chromatin interactions associated to gene co-regulation. By

442 these means, they contribute to proper plant development, a process in which H3K27me3 is a key
443 regulator of global and local facultative heterochromatin topology.

444 **Methods**

445 **Plant material and growth conditions**

446 Plant lines used in this study were in *Arabidopsis thaliana* ecotype Columbia (Col-0) background. The T-
447 DNA insertional mutants *clf-29* (SALK_N521003) and *ref6-5* mutant (GABI_705E03) was obtained from
448 the GABI-Kat collection (Mirouze et al. 2012) were used. Seeds were surface-sterilized by treatment with
449 bayrochlore, washed, and then sown in sterile half-strength MS medium, placed for 2–4 days at 4 °C to
450 obtain homogeneous germination, and plants were grown in a vertical orientation in square petri dishes
451 in growth chambers at 20 °C under long-day (16 h of light) conditions.

452

453 **Immunostaining**

454 Immunofluorescence labelling was performed according to Latrasse et al (Latrasse et al. 2017). Briefly,
455 seedlings of 14-day-old *Arabidopsis* were fixed and then nuclei were isolated, placed on a poly-lysine
456 slide and incubated overnight at 4 °C with primary antibodies specific to lysine-9-acetylated H3 (Millipore
457 07-352) and lysine-27-trimethylated H3 (Millipore 07-449). After washing, slides were incubated for 1h at
458 room temperature in the dark either with Goat anti-Rabbit Alexa Fluor Plus 488 (A11034 Invitrogen) and
459 Goat anti-Mouse Alexa Fluor Plus 555 (A32727 Invitrogen) or with Goat anti-Rabbit Alexa Fluor Plus 555
460 (A32732 Invitrogen) and Goat anti-Mouse Alexa Fluor Plus 488 (A32723 Invitrogen) as secondary
461 antibodies. DNA was counterstained with 4,6 diamidino-2-phenylindole (DAPI) in SlowFade Diamond
462 Antifade mounting media. Slides were directly imaged on a confocal microscope (Zeiss Microsystems).

463

464 **Chromatin Immunoprecipitation followed by high-throughput sequencing (ChIP-seq) assay**

465 ChIP-seq assays were performed on shoot or root of 14-day-old seedlings using anti-H3K27me3

466 (Millipore 07–449). Plant material was cross-linked in 1% (v/v) formaldehyde at room temperature for 15
467 min. Cross-linking was quenched with 0.125 M glycine for 5 min. The cross-linked plantlets were ground
468 and nuclei were isolated and lysed in Nuclei Lysis Buffer (0.1% SDS, 50 mM Tris-HCl pH 8, 10 mM
469 ethylene diamine tetraacetic acid (EDTA) pH 8). Cross-linked chromatin was sonicated for 5 min using a
470 Covaris S220 (Peak Power: 175, cycles/burst: 200. Duty Factory: 20). The complexes were
471 immunoprecipitated with antibodies, overnight at 4°C with gentle shaking, and incubated for 1 h at 4°C
472 with 40 µl of Dynabeads Protein A (Thermo Fisher Scientific). The beads were washed 2 × 5 min in ChIP
473 Wash Buffer 1 (0.1% SDS, 1% Triton X-100, 20 mM Tris-HCl pH 8, 2 mM EDTA pH 8, 150 mM NaCl), 2 × 5
474 min in ChIP Wash Buffer 2 (0.1% SDS, 1% Triton X-100, 20 mM Tris-HCl pH 8, 2 mM EDTA pH 8, 500 mM
475 NaCl), 2 × 5 min in ChIP Wash Buffer 3 (0.25 mM LiCl, 1% NP-40, 1% sodium deoxycholate, 10 mM
476 Tris-HCl pH 8, 1 mM EDTA pH 8) and twice in TE (10 mM Tris-HCl pH 8, 1 mM EDTA pH 8). ChIPed DNA
477 was eluted by two 15-min incubations at 65°C with 250 µl of Elution Buffer (1% SDS, 0.1 M NaHCO₃).
478 Chromatin was reverse-cross-linked by adding 20 µl of NaCl 5 M and incubated overnight at 65°C.
479 Reverse cross-linked DNA was submitted to RNase and Proteinase K treatment, and extracted with
480 phenol–chloroform. DNA was ethanol precipitated in the presence of 20 µg of glycogen and resuspended
481 in 10 µl of nuclease-free water in a DNA low-bind tube. Libraries were then generated using 10 ng of DNA
482 and NEBNext Ultra II DNA Library Prep Kit for Illumina (NEB). The quality of the libraries was assessed
483 with Agilent 2100 Bioanalyzer (Agilent), and the libraries were subjected to 1 × 75 bp high-throughput
484 sequencing by NextSeq 500 (Illumina).

485

486 **HiChIP assay**

487 HiChIP experiments were performed on shoots and roots of 14-day-old seedlings using the same
488 procedure as in Concia et al (Concia et al. 2020) with either anti-H3K9ac (Millipore 07–352) or anti-
489 H3K27me3 (Millipore 07–449). The quality of the libraries was assessed with Agilent 2100 Bioanalyzer

490 (Agilent), and the libraries were subjected to 2×75 bp paired-end high-throughput sequencing by
491 NextSeq 500 (Illumina).

492

493 **Capture Hi-C assay**

494 For capture Hi-C, in situ Hi-C libraries from shoot and root of Col-0, *ref6*, and *clf* were first generated as in
495 Concia et al (Concia et al. 2020). The quality and the DNA concentration of the libraries were assessed
496 with Agilent 2100 Bioanalyzer (Agilent). Capture was then performed using SureSelect XT Target
497 Enrichment System for Illumina Paired-End Multiplexed Sequencing Library (Agilent) according to
498 manufacturer's recommendation. To this end, 52911 custom probes were designed, covering 2.658 Mbp
499 and 4650 genes (Supplemental Table S25). Capture was performed using 1 μ g of in situ Hi-C libraries and
500 following manufacturer's recommendation. Quality control and sequencing of the libraries were done in
501 the same way as for HiChIP assays.

502

503 **Analysis of CHIP-seq data**

504 Single-end sequencing of ChIP samples was performed using Illumina NextSeq 500 with a read length of
505 76 bp. Trimmomatic-0.38 (Martin 2011) was used for quality trimming. Parameters for read quality
506 filtering were set as follows: Minimum length of 36 bp; Mean Phred quality score greater than 30;
507 Leading and trailing bases removal with base quality <5. The reads were mapped onto the TAIR10
508 assembly using Bowtie 2 (Langmead and Salzberg 2012) with mismatch permission of 1 bp. To identify
509 significantly enriched regions, we used MACS2 (Gaspar 2018) Parameters for peaks detection were set as
510 follows: Number of duplicate reads at a location:1; mfold of 5:50; q-value cutoff: 0.05; extsize 200; broad
511 peak. To extract the average scores across the genomic regions, multiBigwigSummary command from
512 the deepTools package (Ramírez et al. 2016) was used with default parameters on the RPGC normalized
513 bigWig files.

514 **Differential expression analysis**

515 Single-end sequencing of RNA-seq samples were trimmed using Trimmomatic-0.38 with the parameters:
516 Minimum length of 30 bp; Mean Phred quality score greater than 30; Leading and trailing bases removal
517 with base quality <5. STAR aligner (Dobin et al. 2013) was used to mapped the reads to TAIR10 genome
518 assembly. Raw read counts were then extracted using featureCounts based on the gene annotations in
519 Araport11_GFF3_genes_transposons.201606.gtf. Finally, we used DESeq2 (Love et al. 2014) to identify
520 differentially expressed genes. Genes having read counts ≥ 50 in atleast 2 samples were considered for
521 differential expression analysis.

522

523 **Analysis of HiChIP and Capture Hi-C data**

524 Raw FASTQ files were preprocessed with Trimmomatic-0.38 to remove Illumina sequencing adapters.
525 The 5' and 3' ends with a quality score below 5 (Phred+33) were trimmed and reads shorter than 30 bp
526 after trimming were dropped. The trimmed files were then processed with HiC-Pro v2.11.1 (Servant et al.
527 2015). The reads were aligned using Bowtie 2 onto the TAIR10 assembly with default settings, except for
528 the parameter "--score-min L, -0.6, -0.8". Invalid ligation products (such as dangling ends, fragments
529 ligated on themselves, and ligations of juxtaposed fragments) were discarded. Valid pairs were used to
530 produce raw interaction matrixes at various resolutions. Finally, ".hic" files were generated with the
531 software Juicer Tools and visualized with the tool Juicebox (Durand et al. 2016).

532

533 **Identification and analysis of genomic interactions**

534 Valid pairs generated are further analysed using HOMER v4.10 (Zhang et al. 2008) for different
535 resolutions (500bp for short range interactions and 20kb for long range interactions). For the short range
536 interactions, both the anchors of the interactions (genomic bins) were annotated with genes using
537 BEDTools intersect. We removed interactions without any gene annotations, self-loops and duplicates.

538 Finally, based on the gene annotations, we integrated the log fold-change from RNA-seq data and CHIP-
539 seq data.

540

541 **Data access**

542 All raw and processed sequencing data generated in this study have been submitted to the NCBI Gene
543 Expression Omnibus (GEO; <https://www.ncbi.nlm.nih.gov/geo/query/acc.cgi>) under accession number
544 GSE155502.

545

546 **Competing interest statement**

547 The authors declare no competing interests.

548

549 **Acknowledgments**

550 This work was supported by the Agence National de la Recherche ANR (3DWheat project ANR-19-CE20-
551 0001-01) and by the Institut Universitaire de France (IUF).

552 Y.H. was supported by China Scholar Council fellowships (201806690005).

553

554 **Author contributions**

555 M.B. designed this research project. Y.H., J.R. N.R.G. and R.B. collected the plant materials. Y.H. and D.L.
556 performed the Capture Hi-C, HiChIP, ChIP-seq experiments and Capture Hi-C, HiChIP, ChIP-seq libraries.

557 D.L. performed the Illumina sequencing and Immunofluorescence staining experiments. S.S., J.R, D.M,

558 J.A., D.L, L.C. and M.B. performed the bioinformatics analyses. Y.H., S.S., D.L. and M.B. made figures and

559 supplement data. M.B. F.A and J.R wrote the paper with support from all authors. M.M, S.A, A.V.P, F.B,

560 C.B., F.A, H.H., M.C., J.G.M., C.R., D.L analyzed the data and provided critical feedback. The authors read

561 and approved the final manuscript.

562 **References**

- 563 Ahmad A, Zhang Y, Cao X. 2010. Decoding the Epigenetic Language of Plant Development. *Mol Plant* **3**:
564 719–728.
- 565 Antunez-Sanchez J, Naish M, Ramirez-Prado JS, Ohno S, Huang Y, Dawson A, Opasathian K, Manza-
566 Mianza D, Ariel F, Raynaud C, et al. 2020. A new role for histone demethylases in the maintenance
567 of plant genome integrity. *Elife* **9**: 1–32.
- 568 Bantignies F, Roure V, Comet I, Leblanc B, Schuettengruber B, Bonnet J, Tixier V, Mas A, Cavalli G. 2011.
569 Polycomb-dependent regulatory contacts between distant hox loci in drosophila. *Cell* **144**: 214–226.
- 570 Berry S, Rosa S, Howard M, Bühler M, Dean C. 2017. Disruption of an RNA-binding hinge region abolishes
571 LHP1-mediated epigenetic repression. *Genes Dev* **31**: 2115–2120.
- 572 Boettiger AN, Bintu B, Moffitt JR, Wang S, Beliveau BJ, Fudenberg G, Imakaev M, Mirny LA, Wu CT,
573 Zhuang X. 2016. Super-resolution imaging reveals distinct chromatin folding for different epigenetic
574 states. *Nature* **529**: 418–422.
- 575 Cheng K, Xu Y, Yang C, Ouellette L, Niu L, Zhou X, Chu L, Zhuang F, Liu J, Wu H, et al. 2020. Histone tales:
576 Lysine methylation, a protagonist in Arabidopsis development. *J Exp Bot* **71**: 793–807.
- 577 Cheutin T, Cavalli G. 2014. Polycomb silencing: From linear chromatin domains to 3D chromosome
578 folding. *Curr Opin Genet Dev* **25**: 30–37.
- 579 Choi J, Strickler SR, Richards EJ. 2019. Loss of CRWN nuclear proteins induces cell death and salicylic acid
580 defense signaling. *Plant Physiol* **179**: 1315–1329.
- 581 Concia L, Veluchamy A, Ramirez-Prado JS, Martin-Ramirez A, Huang Y, Perez M, Domenichini S,
582 Rodriguez-Granados NY, Kim S-K, Blein T, et al. 2020. Wheat chromatin architecture is organized in
583 genome territories and transcription factories. *Genome Biol* **ACCEPTED**.
- 584 de Wit E, Vos ESM, Holwerda SJB, Valdes-Quezada C, Verstegen MJAM, Teunissen H, Splinter E, Wijchers
585 PJ, Krijger PHL, de Laat W. 2015. CTCF Binding Polarity Determines Chromatin Looping. *Mol Cell* **60**:

586 676–684.

587 Dekker J, Heard E. 2015. Structural and functional diversity of Topologically Associating Domains. *FEBS*

588 *Lett* **589**: 2877–2884.

589 Dixon JR, Gorkin DU, Ren B. 2016. Chromatin Domains: The Unit of Chromosome Organization. *Mol Cell*

590 **62**: 668–680.

591 Dixon JR, Selvaraj S, Yue F, Kim A, Li Y, Shen Y, Hu M, Liu JS, Ren B. 2012. Topological domains in

592 mammalian genomes identified by analysis of chromatin interactions. *Nature* **485**: 376–380.

593 Dobin A, Davis CA, Schlesinger F, Drenkow J, Zaleski C, Jha S, Batut P, Chaisson M, Gingeras TR. 2013.

594 STAR: Ultrafast universal RNA-seq aligner. *Bioinformatics* **29**: 15–21.

595 Dong P, Tu X, Chu PY, Lü P, Zhu N, Grierson D, Du B, Li P, Zhong S. 2017a. 3D Chromatin Architecture of

596 Large Plant Genomes Determined by Local A/B Compartments. *Mol Plant* **10**: 1497–1509.

597 <https://doi.org/10.1016/j.molp.2017.11.005> (Accessed January 2, 2021).

598 Dong P, Tu X, Chu PY, Lü P, Zhu N, Grierson D, Du B, Li P, Zhong S. 2017b. Comprehensive mapping of

599 long range interactions reveals folding principles of the human genome. *Mol Plant* **10**: 1497–1509.

600 Dong Q, Li N, Li X, Yuan Z, Xie D, Wang X, Li J, Yu Y, Wang J, Ding B, et al. 2018. Genome-wide Hi-C

601 analysis reveals extensive hierarchical chromatin interactions in rice. *Plant J* **94**: 1141–1156.

602 Du Z, Zheng H, Kawamura YK, Zhang K, Gassler J, Powell S, Xu Q, Lin Z, Xu K, Zhou Q, et al. 2020.

603 Polycomb Group Proteins Regulate Chromatin Architecture in Mouse Oocytes and Early Embryos.

604 *Mol Cell* **77**: 825-839.e7.

605 Durand NC, Robinson JT, Shamim MS, Machol I, Mesirov JP, Lander ES, Lieberman E, Correspondence A.

606 2016. Juicebox Provides a Visualization System for Hi-C Contact Maps with Unlimited Zoom. *Cell*

607 *Syst* **3**: 99–101.

608 Eichten SR, Schmitz RJ, Springer NM. 2014. Epigenetics: Beyond Chromatin Modifications and Complex

609 Genetic Regulation. *Plant Physiol* **165**: 933–947.

610 El-Sharnouby S, Fischer B, Magbanua JP, Umans B, Flower R, Choo SW, Russell S, White R. 2017. Regions
611 of very low H3K27me3 partition the Drosophila genome into topological domains. *PLoS One* **12**: 1–
612 23.

613 Eskeland R, Leeb M, Grimes GR, Kress C, Boyle S, Sproul D, Gilbert N, Fan Y, Skoultchi AI, Wutz A, et al.
614 2010. Ring1B Compacts Chromatin Structure and Represses Gene Expression Independent of
615 Histone Ubiquitination. *Mol Cell* **38**: 452–464.

616 Feng S, Cokus SJ, Schubert V, Zhai J, Pellegrini M, Jacobsen SE. 2014. Genome-wide Hi-C Analyses in Wild-
617 Type and Mutants Reveal High-Resolution Chromatin Interactions in Arabidopsis. *Mol Cell* **55**: 694–
618 707. [/pmc/articles/PMC4347903/?report=abstract](https://pubmed.ncbi.nlm.nih.gov/24781111/) (Accessed January 10, 2021).

619 Fortin JP, Hansen KD. 2015. Reconstructing A/B compartments as revealed by Hi-C using long-range
620 correlations in epigenetic data. *Genome Biol* **16**: 1–23.

621 Francis NJ, Kingston RE, Woodcock CL. 2004. Chromatin compaction by a polycomb group protein
622 complex. *Science (80-)* **306**: 1574–1577.

623 Fullwood MJ, Liu MH, Pan YF, Liu J, Xu H, Mohamed Y Bin, Orlov YL, Velkov S, Ho A, Mei PH, et al. 2009.
624 An oestrogen-receptor- α -bound human chromatin interactome. *Nature* **462**: 58–64.

625 Gambino G, Pantaleo V. 2017. Epigenetics in plant-pathogen interactions. In *Plant Epigenetics* (ed. J.B.
626 Nikolaus Rajewsky, Stefan Jurga), pp. 385–404, Springer Nature, Cham, Switzerland.

627 Gaspar J. 2018. Improved peak-calling with MACS2. *bioRxiv* 496521.

628 Gaudin V, Libault M, Pouteau S, Juul T, Zhao G, Lefebvre D, Grandjean O. 2001. Mutations in LIKE
629 HETEROCHROMATIN PROTEIN 1 affect flowering time and plant architecture in Arabidopsis.
630 *Development* **128**: 4847–58.

631 Gonzalez-Sandoval A, Gasser SM. 2016. On TADs and LADs: Spatial Control Over Gene Expression. *Trends*
632 *Genet* **32**: 485–495.

633 Grob S, Schmid MW, Grossniklaus U. 2014. Hi-C Analysis in Arabidopsis Identifies the KNOT, a Structure

634 with Similarities to the flamenco Locus of *Drosophila*. *Mol Cell* **55**: 678–693.

635 Grossniklaus U, Paro R. 2014. Transcriptional Silencing by Polycomb Group proteins. *Cold Spring Harb*
636 *Perspect Biol* **6**: 1–20.

637 Guo Y, Xu Q, Canzio D, Shou J, Li J, Gorkin DU, Jung I, Wu H, Zhai Y, Tang Y, et al. 2015. CRISPR Inversion
638 of CTCF Sites Alters Genome Topology and Enhancer/Promoter Function. *Cell* **162**: 900–910.

639 Ha M, Ng DW, Li W, Chen ZJ. 2011. Coordinated histone modifications are associated with gene
640 expression variation within and between species. 590–598.

641 Hernández-Muñoz I, Taghavi P, Kuijl C, Neefjes J, van Lohuizen M. 2005. Association of BMI1 with
642 Polycomb Bodies Is Dynamic and Requires PRC2/EZH2 and the Maintenance DNA
643 Methyltransferase DNMT1. *Mol Cell Biol* **25**: 11047–11058.

644 Hou X, Zhou J, Liu C, Liu L, Shen L, Yu H. 2014. Nuclear factor Y-mediated H3K27me3 demethylation of
645 the SOC1 locus orchestrates flowering responses of *Arabidopsis*. *Nat Commun* **5**: 1–14.

646 Hu B, Wang N, Bi X, Karaaslan ES, Weber AL, Zhu W, Berendzen KW, Liu C. 2019. Plant lamin-like proteins
647 mediate chromatin tethering at the nuclear periphery. *Genome Biol* **20**: 1–18.

648 Huang Y, Rodriguez-Granados NY, Latrasse D, Raynaud C, Benhamed M, Ramirez-Prado JS. 2020. The
649 matrix revolutions: towards the decoding of the plant chromatin three-dimensional reality. *J Exp*
650 *Bot* **71**: 5129–5147.

651 Illingworth RS. 2019. Chromatin folding and nuclear architecture: PRC1 function in 3D. *Curr Opin Genet*
652 *Dev* **55**: 82–90.

653 Joshi O, Wang SY, Kuznetsova T, Atlasi Y, Peng T, Fabre PJ, Habibi E, Shaik J, Saeed S, Handoko L, et al.
654 2015. Dynamic Reorganization of Extremely Long-Range Promoter-Promoter Interactions between
655 Two States of Pluripotency. *Cell Stem Cell* **17**: 748–757.

656 Kaiser VB, Semple CA. 2017. When TADs go bad: chromatin structure and nuclear organisation in human
657 disease. *F1000Research* **6**: 314.

658 Kassis JA, Kennison JA, Tamkun JW. 2017. Polycomb and trithorax group genes in drosophila. *Genetics*
659 **206**: 1699–1725.

660 Kouzarides T. 2007. Chromatin Modifications and Their Function. *Cell* **128**: 693–705.

661 Kundu S, Ji F, Sunwoo H, Jain G, Lee JT, Sadreyev RI, Dekker J, Kingston RE. 2017. Polycomb Repressive
662 Complex 1 Generates Discrete Compacted Domains that Change during Differentiation. *Mol Cell* **65**:
663 432-446.e5.

664 Langmead B, Salzberg SL. 2012. Fast gapped-read alignment with Bowtie 2. *Nat Methods* **9**: 357–359.

665 Lanzaolo C, Roure V, Dekker J, Bantignies F, Orlando V. 2007. Polycomb response elements mediate the
666 formation of chromosome higher-order structures in the bithorax complex. **9**.

667 Latrasse D, Jégu T, Li H, de Zelicourt A, Raynaud C, Legras S, Gust A, Samajova O, Veluchamy A,
668 Rayapuram N, et al. 2017. MAPK-triggered chromatin reprogramming by histone deacetylase in
669 plant innate immunity. *Genome Biol* **18**: 1–19.

670 Lieberman-Aiden E, van Berkum NL, Williams L, Imakaev M, Ragozy T, Telling A, Amit I, Lajoie BR, Sabo
671 PJ, Dorschner MO, et al. 2009. Comprehensive Mapping of Long-Range Interactions Reveals Folding
672 Principles of the Human Genome. *Science (80-)* **326**: 289–293.

673 Liu C, Cheng YJ, Wang JW, Weigel D. 2017. Prominent topologically associated domains differentiate
674 global chromatin packing in rice from Arabidopsis. *Nat Plants* **3**: 742–748.

675 Liu C, Wang C, Wang G, Becker C, Weigel D. 2016a. Genome-wide analysis of chromatin packing in
676 Arabidopsis thaliana at single- gene resolution. *Genome Res* 1–30.

677 Liu J, Deng S, Wang H, Ye J, Wu HW, Sun HX, Chua NH. 2016b. CURLY LEAF regulates gene sets
678 coordinating seed size and lipid biosynthesis. *Plant Physiol* **171**: 424–436.

679 Love MI, Huber W, Anders S. 2014. Moderated estimation of fold change and dispersion for RNA-seq
680 data with DESeq2. *Genome Biol* **15**: 550.

681 Lu F, Cui X, Zhang S, Jenuwein T, Cao X. 2011. Arabidopsis REF6 is a histone H3 lysine 27 demethylase.

682 *Nat Genet* **43**: 715–719.

683 Lupiáñez DG, Kraft K, Heinrich V, Krawitz P, Brancati F, Klopocki E, Horn D, Kayserili H, Opitz JM, Laxova R,
684 et al. 2015. Disruptions of Topological Chromatin Domains Cause Pathogenic Rewiring of Gene-
685 Enhancer Interactions. *Cell* **161**: 1012–1025.

686 Lupiáñez DG, Spielmann M, Mundlos S. 2016. Breaking TADs: How Alterations of Chromatin Domains
687 Result in Disease. *Trends Genet* **32**: 225–237.

688 Mach J. 2018. In the Histone Zone: The Mighty Eraser. *Plant Cell* **30**: 5–6.

689 Martin M. 2011. Cutadapt removes adapter sequences from high-throughput sequencing reads.
690 *EMBnet.journal* **17**: 10.

691 Mascher M, Gundlach H, Himmelbach A, Beier S, Twardziok SO, Wicker T, Radchuk V, Dockter C, Hedley
692 PE, Russell J, et al. 2017. A chromosome conformation capture ordered sequence of the barley
693 genome. *Nature* **544**: 427.

694 McLaughlin K, Flyamer IM, Thomson JP, Mjoseng HK, Shukla R, Williamson I, Grimes GR, Illingworth RS,
695 Adams IR, Pennings S, et al. 2019. DNA Methylation Directs Polycomb-Dependent 3D Genome Re-
696 organization in Naive Pluripotency. *Cell Rep* **29**: 1974-1985.e6.

697 Melé M, Rinn JL. 2016. “Cat’s Cradling” the 3D Genome by the Act of LncRNA Transcription. *Mol Cell* **62**:
698 657–664.

699 Mifsud B, Tavares-Cadete F, Young AN, Sugar R, Schoenfelder S, Ferreira L, Wingett SW, Andrews S, Grey
700 W, Ewels PA, et al. 2015. Mapping long-range promoter contacts in human cells with high-
701 resolution capture Hi-C. *Nat Genet* **47**: 598–606.

702 Mirouze M, Lieberman-Lazarovich M, Aversano R, Bucher E, Nicolet J, Reinders J, Paszkowski J. 2012.
703 Loss of DNA methylation affects the recombination landscape in Arabidopsis. *Proc Natl Acad Sci U S*
704 *A* **109**: 5880–5885. www.pnas.org/lookup/suppl/doi:10.1073/pnas.1120841109/-
705 [/DCSupplemental.5880-5885%7CPNAS%7Cwww.pnas.org/cgi/doi/10.1073/pnas.1120841109](http://DCSupplemental.5880-5885%7CPNAS%7Cwww.pnas.org/cgi/doi/10.1073/pnas.1120841109)

706 (Accessed February 13, 2021).

707 Mishra A, Hawkins RD. 2017. Three-dimensional genome architecture and emerging technologies:
708 looping in disease. *Genome Med* **9**: 87.

709 Misteli T. 2007. Beyond the Sequence: Cellular Organization of Genome Function. *Cell* **128**: 787–800.

710 Mozgova I, Köhler C, Hennig L. 2015. Keeping the gate closed: functions of the polycomb repressive
711 complex PRC2 in development. *Plant J* **83**: 121–132.

712 Mumbach MR, Rubin AJ, Flynn RA, Dai C, Khavari PA, Greenleaf WJ, Chang HY. 2016. HiChIP: Efficient and
713 sensitive analysis of protein-directed genome architecture. *Nat Methods* **13**: 919–922.
714 <https://www.nature.com/articles/nmeth.3999> (Accessed April 22, 2021).

715 Noh B, Lee SS-H, Kim HH-J, Yi G, Shin E-AEA, Lee M, Jung K-JK, Doyle MMR, Amasino RMR, Noh Y-SY.
716 2004. Divergent Roles of a Pair of Homologous Jumonji/Zinc-Finger-Class Transcription Factor
717 Proteins in the Regulation of Arabidopsis Flowering Time. *Plant Cell* **16**: 2601–2613.

718 Nützmann H-W, Doerr D, Ramírez-Colmenero A, Sotelo-Fonseca JE, Wegel E, Stefano M Di, Wingett SW,
719 Fraser P, Hurst L, Fernandez-Valverde SL, et al. 2020. Active and repressed biosynthetic gene
720 clusters have spatially distinct chromosome states. *Proc Natl Acad Sci* **117**: 13800–13809.

721 Ogiyama Y, Schuettengruber B, Papadopoulos GL, Chang JM, Cavalli G. 2018. Polycomb-Dependent
722 Chromatin Looping Contributes to Gene Silencing during Drosophila Development. *Mol Cell* **71**: 73-
723 88.e5. <https://doi.org/10.1016/j.molcel.2018.05.032> (Accessed February 1, 2021).

724 Pachano T, Crispatzu G, Rada-Iglesias A. 2019. Polycomb proteins as organizers of 3D genome
725 architecture in embryonic stem cells. *Brief Funct Genomics* **18**: 358–366.

726 Pfluger J, Wagner D. 2007. Histone modifications and dynamic regulation of genome accessibility in
727 plants. *Curr Opin Plant Biol* **10**: 645–652.

728 Ramírez F, Ryan DP, Grüning B, Bhardwaj V, Kilpert F, Richter AS, Heyne S, Dündar F, Manke T. 2016.
729 deepTools2: a next generation web server for deep-sequencing data analysis. *Nucleic Acids Res* **44**:

730 W160–W165.

731 Rao SSP, Huang S-C, Glenn B, Hilaire S, Casellas R, Lander ES, Lieberman E, Correspondence A. 2017.
732 Cohesin Loss Eliminates All Loop Domains. *Cell* **171**: 305-309.e24.
733 <https://doi.org/10.1016/j.cell.2017.09.026> (Accessed February 1, 2021).

734 Ricci WA, Lu Z, Ji L, Marand AP, Ethridge CL, Murphy NG, Noshay JM, Galli M, Mejía-Guerra MK, Colomé-
735 Tatché M, et al. 2019. Widespread long-range cis-regulatory elements in the maize genome. *Nat*
736 *Plants* **5**: 1237–1249.

737 Rocha PP, Raviram R, Bonneau R, Skok JA. 2015. Breaking TADs: Insights into hierarchical genome
738 organization. *Epigenomics* **7**: 523–526.

739 Rodriguez-Granados NY, Ramirez-Prado JS, Veluchamy A, Latrasse D, Raynaud C, Crespi M, Ariel F,
740 Benhamed M. 2016. Put your 3D glasses on: plant chromatin is on show. *J Exp Bot* **67**: 1–17.

741 Rosa-Garrido M, Chapski DJ, Schmitt AD, Kimball TH, Karbassi E, Monte E, Balderas E, Pellegrini M, Shih T-
742 T, Soehalim E, et al. 2017. High-Resolution Mapping of Chromatin Conformation in Cardiac
743 Myocytes Reveals Structural Remodeling of the Epigenome in Heart Failure. *Circulation* **136**: 1613–
744 1625.

745 Rosencrance CD, Ammouri HN, Yu Q, Ge T, Rendleman EJ, Marshall SA, Eagen KP. 2020. Chromatin
746 Hyperacetylation Impacts Chromosome Folding by Forming a Nuclear Subcompartment. *Mol Cell*
747 **78**: 112-126.e12.

748 Rowley MJ, Corces VG. 2016. The three-dimensional genome: principles and roles of long-distance
749 interactions. *Curr Opin Cell Biol* **40**: 8–14.

750 Rowley MJ, Nichols MH, Lyu X, Ando-Kuri M, Rivera ISM, Hermetz K, Wang P, Ruan Y, Corces VG. 2017.
751 Evolutionarily Conserved Principles Predict 3D Chromatin Organization. *Mol Cell* **67**: 837-852.e7.

752 Schoenfelder S, Sugar R, Dimond A, Javierre BM, Armstrong H, Mifsud B, Dimitrova E, Matheson L,
753 Tavares-Cadete F, Furlan-Magaril M, et al. 2015. Polycomb repressive complex PRC1 spatially

754 constrains the mouse embryonic stem cell genome. *Nat Genet* **47**: 1179–1186.

755 Servant N, Varoquaux N, Lajoie BR, Viara E, Chen CJ, Vert JP, Heard E, Dekker J, Barillot E. 2015. HiC-Pro:
756 An optimized and flexible pipeline for Hi-C data processing. *Genome Biol* **16**: 259.

757 Sutherland H, Bickmore WA. 2009. Transcription factories: gene expression in unions? *Nat Rev Genet* **10**:
758 457–466.

759 Turck F, Roudier F, Farrona S, Martin-Magniette M-LL, Guillaume E, Buisine N, Gagnot S, Martienssen RA,
760 Coupland G, Colot V. 2007. Arabidopsis TFL2/LHP1 Specifically Associates with Genes Marked by
761 Trimethylation of Histone H3 Lysine 27. *PLoS Genet* **3**: 0855–0866.

762 Veluchamy A, Jégu T, Ariel F, Latrasse D, Mariappan KG, Kim S-KK, Crespi M, Hirt H, Bergounioux C,
763 Raynaud C, et al. 2016. LHP1 Regulates H3K27me3 Spreading and Shapes the Three-Dimensional
764 Conformation of the Arabidopsis Genome ed. M. Bendahmane. *PLoS One* **11**: e0158936.

765 Wang C, Liu C, Roqueiro D, Grimm D, Schwab R, Becker C, Lanz C, Weigel D. 2015. Genome-wide analysis
766 of local chromatin packing in Arabidopsis thaliana. *Genome Res* **25**: 246–256.

767 Wang M, Wang P, Lin M, Ye Z, Li G, Tu L, Shen C, Li J, Yang Q, Zhang X. 2018. Evolutionary dynamics of 3D
768 genome architecture following polyploidization in cotton. *Nat Plants* **4**: 90–97.

769 Williamson I, Eskeland R, Lettice LA, Hill AE, Boyle S, Grimes GR, Hill RE, Bickmore WA. 2012. Anterior-
770 posterior differences in HoxD chromatin topology in limb development. *Dev* **139**: 3157–3167.

771 Yan W, Chen D, Smaczniak C, Engelhorn J, Liu H, Yang W, Graf A, Carles CC, Zhou D-X, Kaufmann K. 2018.
772 Dynamic and spatial restriction of Polycomb activity by plant histone demethylases. *Nat Plants* **4**:
773 681–689.

774 Yun M, Wu J, Workman JL, Li B. 2011. Readers of histone modifications. *Cell Res* **21**: 564–578.

775 Zhang X, Germann S, Blus BJ, Khorasanizadeh S, Gaudin V, Jacobsen SE. 2007. The Arabidopsis LHP1
776 protein colocalizes with histone H3 Lys27 trimethylation. *Nat Struct Mol Biol* **14**: 869–71.

777 Zhang Y, Liu T, Meyer CA, Eeckhoutte J, Johnson DS, Bernstein BE, Nussbaum C, Myers RM, Brown M, Li

778 W, et al. 2008. Model-based analysis of ChIP-Seq (MACS). *Genome Biol* **9**: R137.
779 Zheng H, Xie W. 2019. The role of 3D genome organization in development and cell differentiation. *Nat*
780 *Rev Mol Cell Biol* **20**: 535–550.
781 Zhou S, Jiang W, Zhao Y, Zhou DX. 2019. Single-cell three-dimensional genome structures of rice gametes
782 and unicellular zygotes. *Nat Plants* **5**: 795–800.

783

784 **Figure legends**

785 **Figure 1. *Arabidopsis* chromatin organization displays a strong compartmentalization**

786 **(A)** Immunofluorescence detection of H3K9ac (green) and H3K27me3 (red) histone histone modifications
787 and DAPI staining (grey) in an isolated *Arabidopsis* nucleus. Scale bar = 5 μ m. **(B)** Distribution of
788 immunofluorescence signal intensity in the nucleus. The analysis was performed along the white line
789 shown in the merged image in A. **(C)** Visualization of the interaction matrix of Hi-C and HiChIP in a
790 specific region of the Chromosome 2. H3K9ac ChIP-seq signal (blue peaks) were aligned with the maps to
791 highlight the correlation with HiChIP enriched regions as expected. **(D)** Visualization of the interaction
792 matrix of Hi-C and HiChIP in a specific region of the Chromosome 4. H3K27me3 ChIP-seq signal (red
793 peaks) were aligned with the maps to highlight the correlation with HiChIP enriched regions as expected.
794 **(E)** Visualization of the interaction matrix of HiChIP data of H3K9ac and H3K27me3 in a specific region of
795 the Chromosome 2. Dots showing higher (blue) and lower (red) signals in H3K9ac HiChIP compared to
796 H3K27me3 respectively. ChIP-seq signals of H3K9ac (blue peaks) and H3K27me3 (red peaks) were
797 aligned with the map to highlight the correlation with HiChIP enriched regions.

798

799 **Figure 2. Shoot and root nuclei display distinct 3D chromatin architecture**

800 **(A)** Heatmap showing the H3K27me3 HiChIP signal of the top shoot-specific repressive loops (SSRLs). **(B)**
801 Example of long distance SSRL on Chromosome 5. ChIP-seq signals of H3K27me3 in shoot (red peaks) and

802 root (blue peaks) were aligned with the map and the differential analysis of both ChIP-seq signals in
803 differentially interacting regions are highlighted (bottom panels in grey). **(C)** Example of short distance
804 SSRL. H3K27me3 ChIP-seq signal is represented by red peaks and chromatin interactions signal by blue
805 lines. **(D)** Analysis of H3K27me3 levels on SSRLs. The pie chart represents the percentage of the genes
806 involved in SSRLs that are either hyper-methylated in shoot or in root. The boxplot shows the H3K27me3
807 levels in shoot or root of the 47% of shoot hyper-methylated genes involved in SSRLs. **(E)** Scatterplot of
808 \log_2 (shoot/root gene expression fold change) for pairs of genes interacting through H3K27me3-
809 associated contacts in shoot. **(F)** Gene Ontology enrichment analysis of the differentially expressed genes
810 involved in SSRLs. **(G)** Heatmap of H3K27me3 HiChIP signal of the top root specific repressive loops
811 (RSRLs). **(H)** Example of long distance RSRLs on Chromosome 1. ChIP-seq signals of H3K27me3 in shoot
812 (red peaks) and root (blue peaks) were aligned with the map and the differential analysis of both ChIP-
813 seq signals in differentially interacting regions are highlighted (bottom panels in grey). **(I)** Example of
814 short distance RSRLs. **(J)** Analysis of H3K27me3 level over RSRLs. The pie chart represents the percentage
815 of genes involved in RSRLs that are either hyper-methylated in shoot or root. The boxplot displayed the
816 H3K27me3 levels of the 48% of root hyper-methylated genes involved in RSRLs. **(K)** Scatterplot of \log_2
817 (shoot/root gene expression fold change) for pairs of genes interacting through H3K27me3-associated
818 contacts in root. **(L)** Gene Ontology enrichment analysis of the differentially expressed genes involved in
819 RSRLs.

820

821 **Figure 3. The levels of H3K27me3 correlate with the stability of repressive loops**

822 **(A)** Visualization of the interaction matrix of Hi-C and C-Hi-C in a specific region of the Chromosome 1.
823 **(B)** Example of interaction analysis using C-Hi-C data showing captured regions (green bars), H3K27me3
824 ChIP-seq signal (red peaks) and chromatin interactions (purple lines). **(C)** Heatmap of C-Hi-C data
825 showing the shoot specific loops (SSLs). **(D)** Examples of shoot specific interacting region detected by

826 both C-Hi-C and H3K27me3 HiChIP. Probes used for the C-Hi-C are represented by green bars, the
827 H3K27me3 ChIP-seq signal by red peaks, the C-Hi-C interaction signals by purple lines and H3K27me3
828 HiChIP interaction signals by blue lines. **(E)** Venn diagram representing overlap of loops called from
829 HiChIP and C-Hi-C library sets. Only loops containing specific probes were selected for the comparison in
830 HiChIP. **(F)** Pie chart representing the proportion of genes involved in shoot-specific loops that are
831 repressed in shoot (blue, 67%), repressed genes in root (red, 24%) and unchanged (grey, 9%) among the
832 genes involved in loops detected both with HiChIP and C-Hi-C. **(G)** Heatmap of C-Hi-C data showing the
833 top root specific loops (RSLs). **(H)** Examples of root specific interacting region detected by both C-Hi-C
834 and H3K27me3 HiChIP. Probes used for the C-Hi-C are represented by green bars, the H3K27me3 ChIP-
835 seq signal by red peaks, the C-Hi-C interaction signals by purple lines and H3K27me3 HiChIP interaction
836 signals by blue lines. **(I)** Venn diagram representing overlap of loops called from HiChIP and C-Hi-C library
837 sets. Only loops containing specific probes were selected for the comparison in HiChIP. **(J)** Pie chart
838 representing of genes involved in root-specific loops that are repressed in shoot (blue, 35%), repressed
839 genes in root (red, 54%) and unchanged (grey, 11%) among the genes involved in loops detected both
840 with HiChIP and C-Hi-C.

841

842 **Figure 4. Ectopic deposition of H3K27me3 leads to formation of new chromatin repressive loops**

843 **(A)** Schema illustrating the antagonistic role of the PRC2 complex (involving the histone
844 methyltransferase CLF) and the histone demethylase REF6 to control H3K27me3 homeostasis and
845 chromatin remodelling. **(B)** Heatmap of Capture Hi-C (C-Hi-C) data showing *ref6-5* specific loops (reSLs).
846 **(C)** Examples of reSLs detected by C-Hi-C. C-Hi-C interaction signal (blue lines) and H3K27me3 ChIP-seq
847 signal in wild-type (black peaks) and *ref6-5* (red peaks) are represented. **(D)** Model of chromatin contacts
848 organization in wild-type and *ref6-5* mutant. **(E)** Histogram representing the percentage of genes
849 (observed O or expected E) involved in reSLs that are either hyper- or hypo- methylated in *ref6-5*

850 compare to WT. To obtain the expected proportion, we shuffled the H3K27me3 signals 1000 times to
851 obtain the randomized gene counts. The mean of the 1000 permutations was used to determine the
852 expected proportions. The bottom pie chart represents the percentage of *ref6-5* hyper-methylated
853 genes involved in reSLs. The boxplot displays the H3K27me3 levels of the 40% of *ref6-5* hyper-
854 methylated genes involved on reSLs. **(F)** Scatterplot of \log_2 (*ref6-5*/wild-type gene expression fold
855 change) for pairs of genes interacting specifically in *ref6-5* compared to wild-type.

856

857 **Figure 5. Reduction of H3K27me3 levels induces a reconfiguration of chromatin architecture**

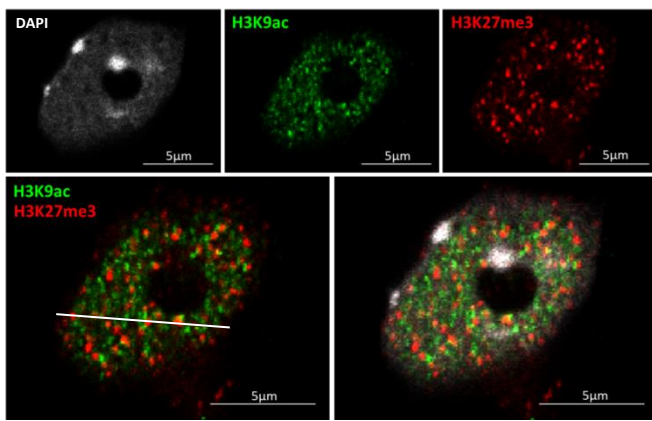
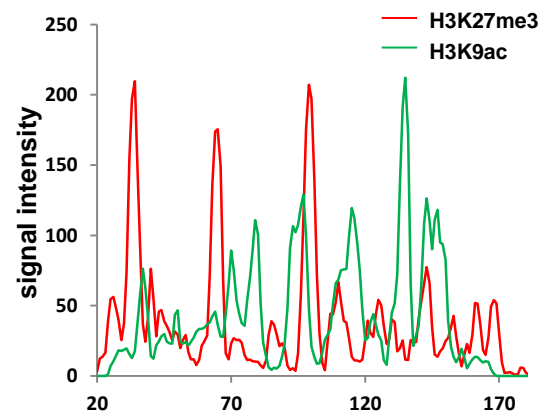
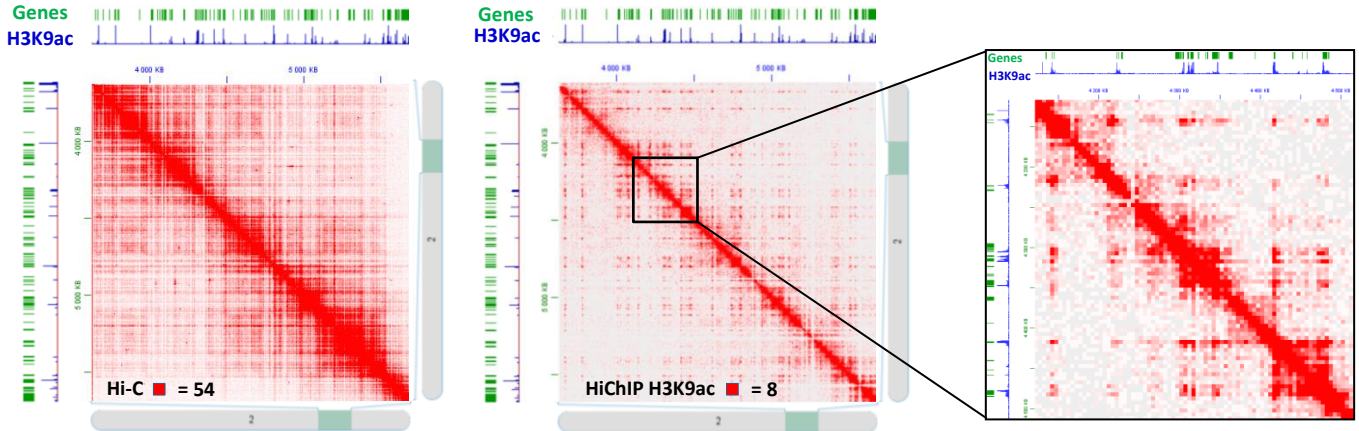
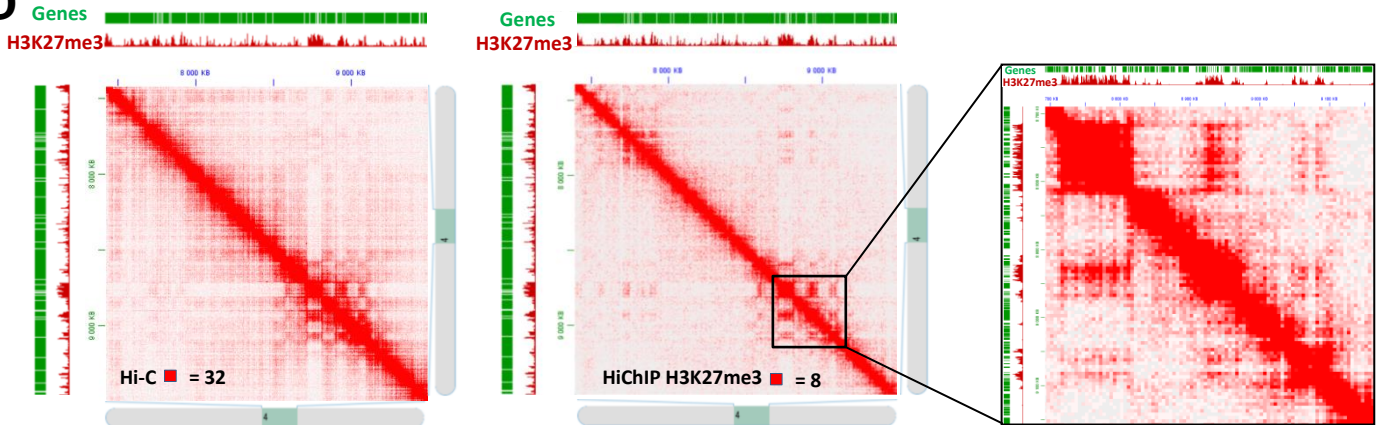
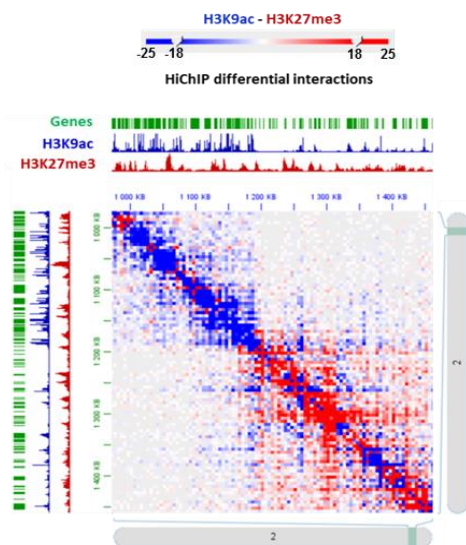
858 **(A)** Heatmap of Capture Hi-C (C-Hi-C) data showing loops that are weaker in *clf* mutant than in wild-type.
859 **(B)** Example of C-Hi-C interactions displaying disrupted loops in *clf* compared to wild-type. C-Hi-C
860 interactions (blue lines) and H3K27me3 ChIP-seq signal in wild-type (red peaks) and *clf* (purple peaks) are
861 represented. **(C)** Histogram representing the percentage of genes (Observed O or Expected E) involved in
862 cSDLs that are either hyper- or hypo- methylated in *clf* compared to WT. To obtain the expected
863 proportion, we shuffled the H3K27me3 signals 1000 times to obtain the randomized gene counts. The
864 mean of the 1000 permutations was used to determine the expected proportions. **(D)** The boxplot
865 displays the H3K27me3 levels of the 40% of *clf* hypo-methylated genes involved in cSDLs. **(E)** The pie
866 chart represents the percentage of *clf* hypo-methylated genes involved in cSDLs. **(F)** Model of chromatin
867 contacts organization in wild-type and *clf* mutant. **(G)** Scatterplot of \log_2 (*clf*/wild-type gene expression
868 fold change) for pairs of genes interacting specifically in wild-type compared to *clf*. **(H)** Heatmap
869 presenting the \log_2 of odd ratios of combinations of features of interacting genes (see Results). Positive
870 \log_2 (odd ratio) indicates enrichment and negative indicates depletion. **(I)** Pie chart representing the
871 proportion of loops involving a gene H3K27me3 hypomethylated and a gene marked or not by H3K9ac in
872 *clf* mutant. Hypo-H3K27me3—No H3K9Ac Loops in *clf* mutant (blue: 40% observed and 61% expected
873 respectively), Hypo-H3K27me3—H3K9Ac Loops (red: 60% observed and 39% expected respectively). **(J)**

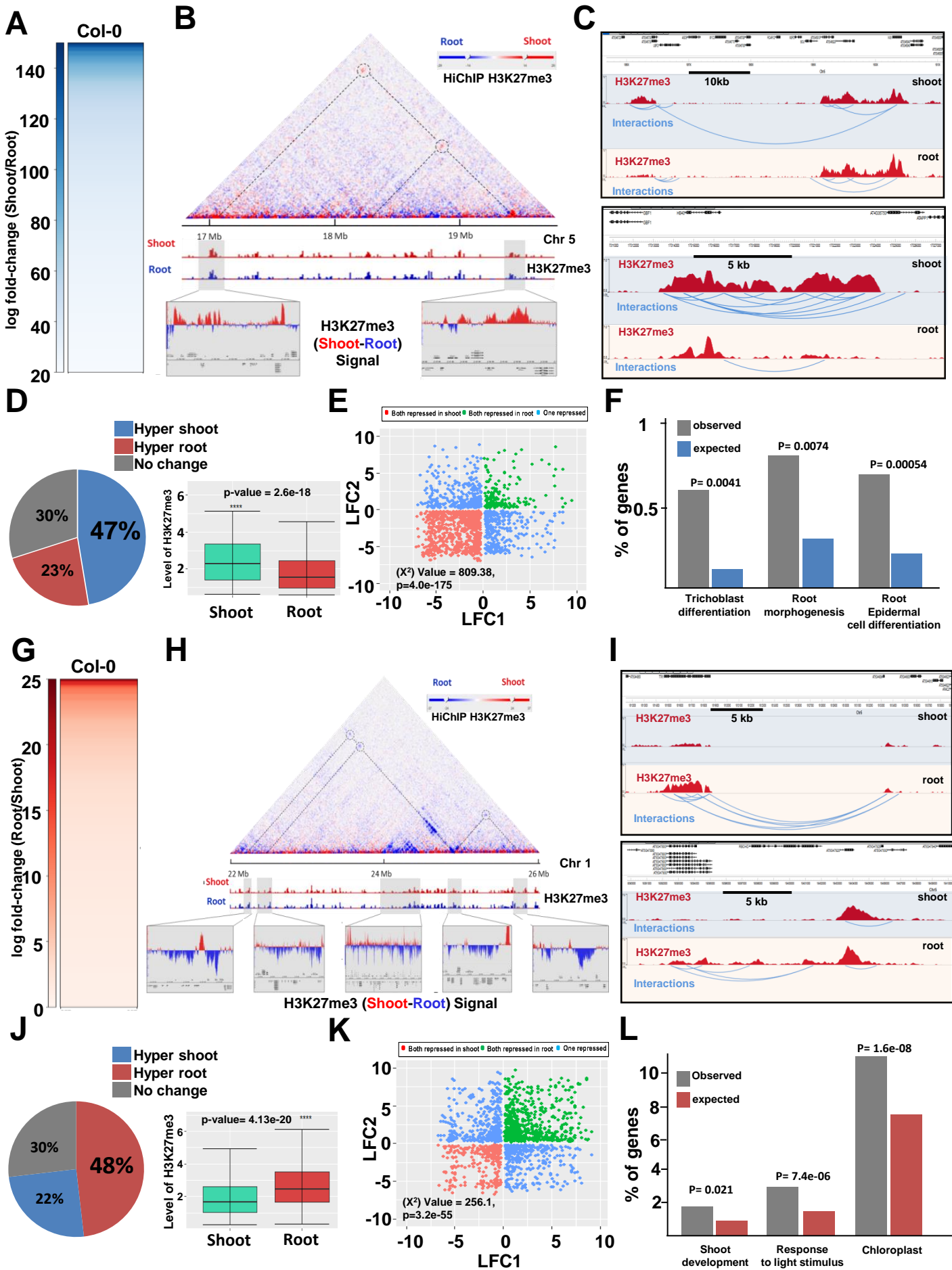
874 Examples of C-Hi-C interactions of a region losing H3K27me3 in *clf* and that tend to establish interactions
875 with regions marked with H3K9ac euchromatin histone modification. C-Hi-C interactions (blue lines),
876 H3K9ac ChIP-seq signal in wild-type and *clf* (green peaks), H3K27me3 ChIP-seq signal in wild-type and *clf*
877 (red peaks) are represented. **(K)** Model of chromatin contacts organization in wild-type and *clf* mutant.

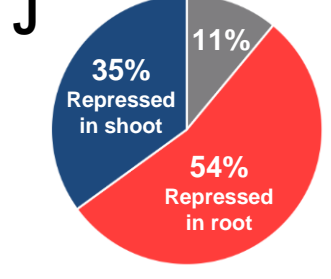
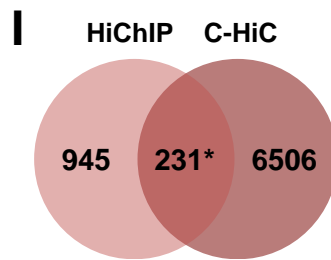
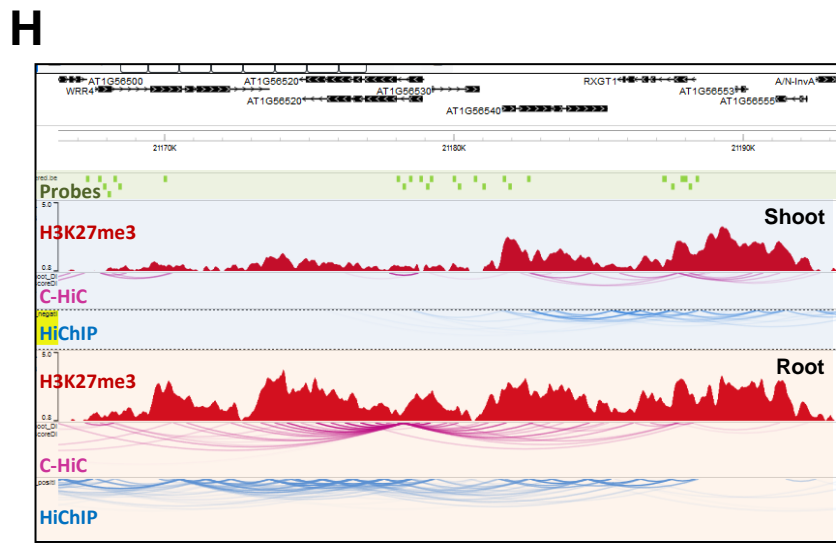
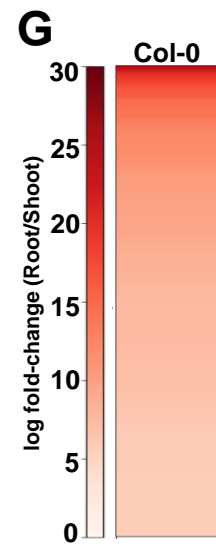
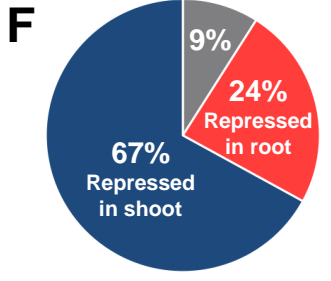
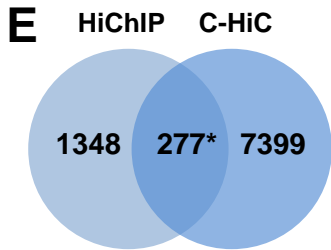
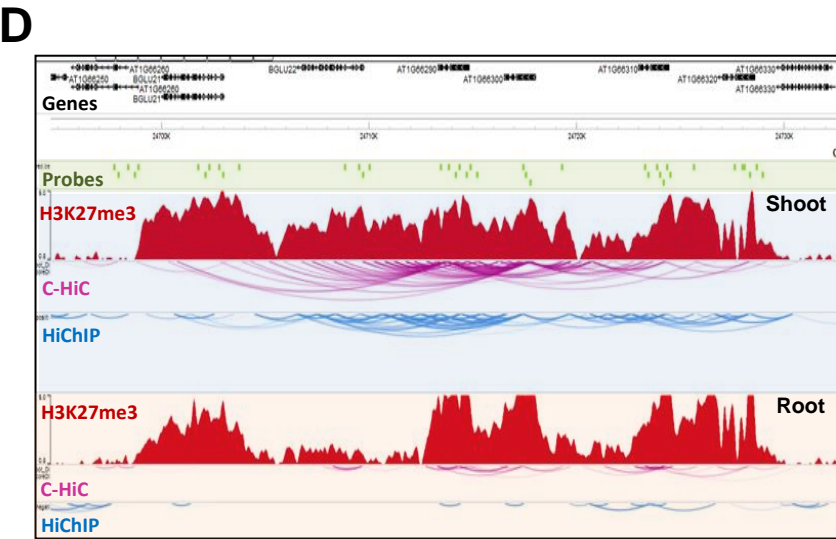
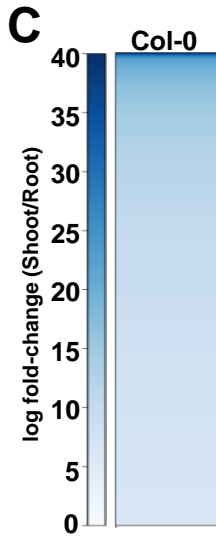
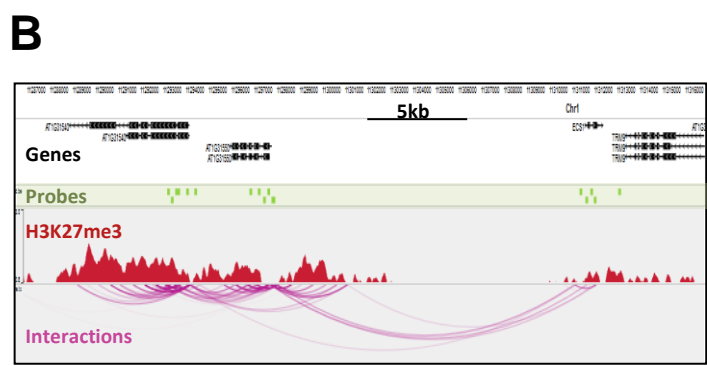
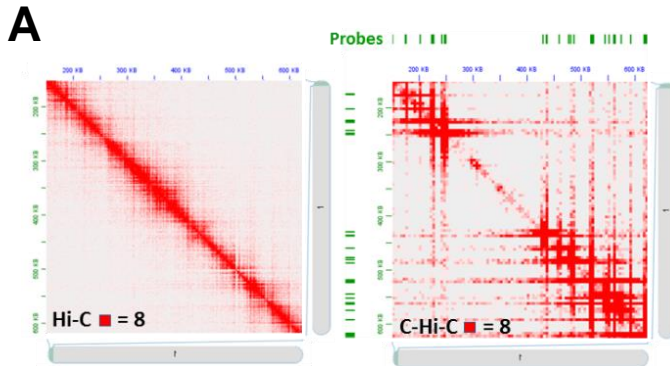
878

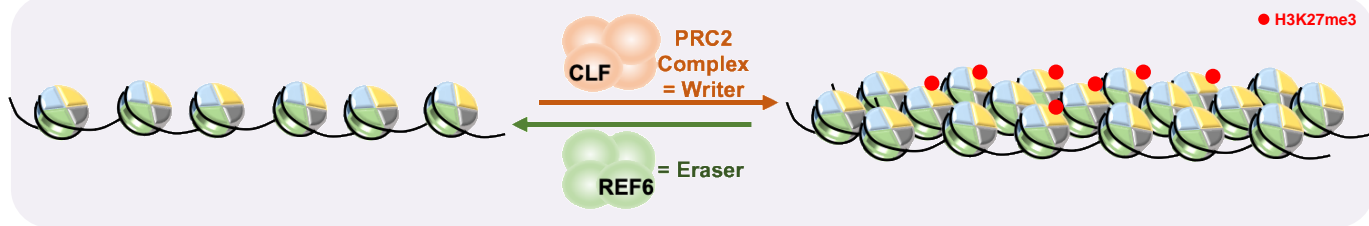
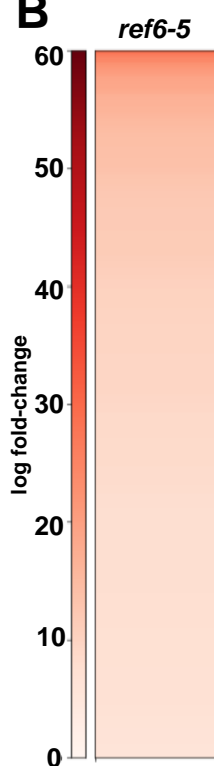
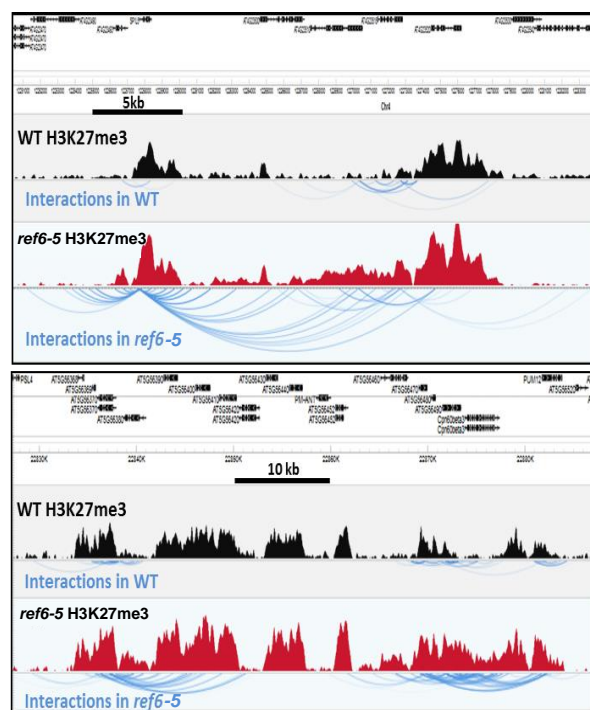
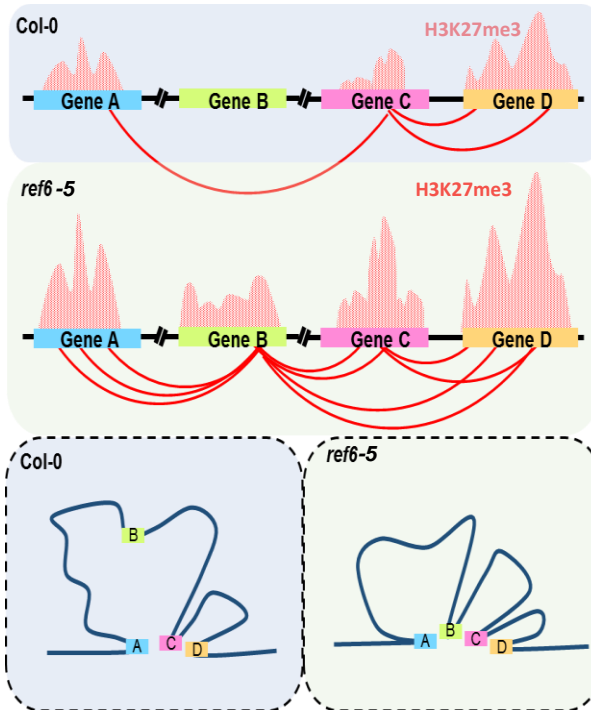
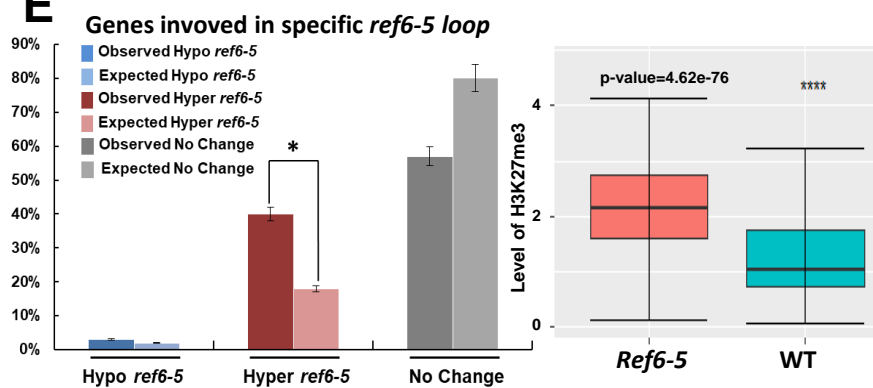
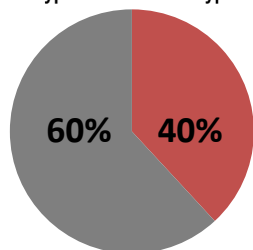
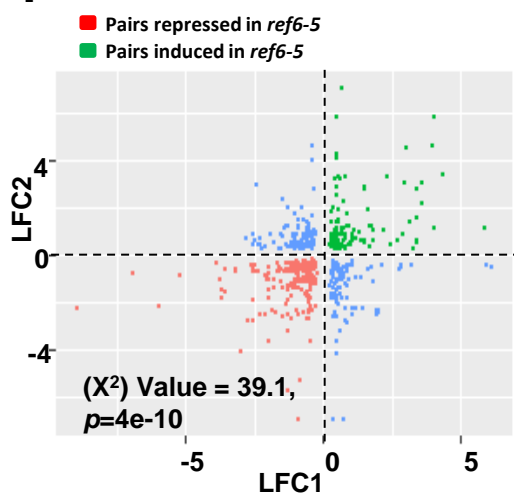
879 **Figure 6. Histone modifiers control chromatin architecture by triggering formation of chromatin**
880 **repressive or active domains to allow gene co-regulation.**

881 Model of the formation of tissue-specific active and repressive chromatin domains in *Arabidopsis*
882 seedlings. The green structures represent active compartments, which are associated with H3K9ac-
883 marked euchromatin. The pink structures represent PcG-repressive compartments which are associated
884 with H3K27me3-marked facultative heterochromatin.

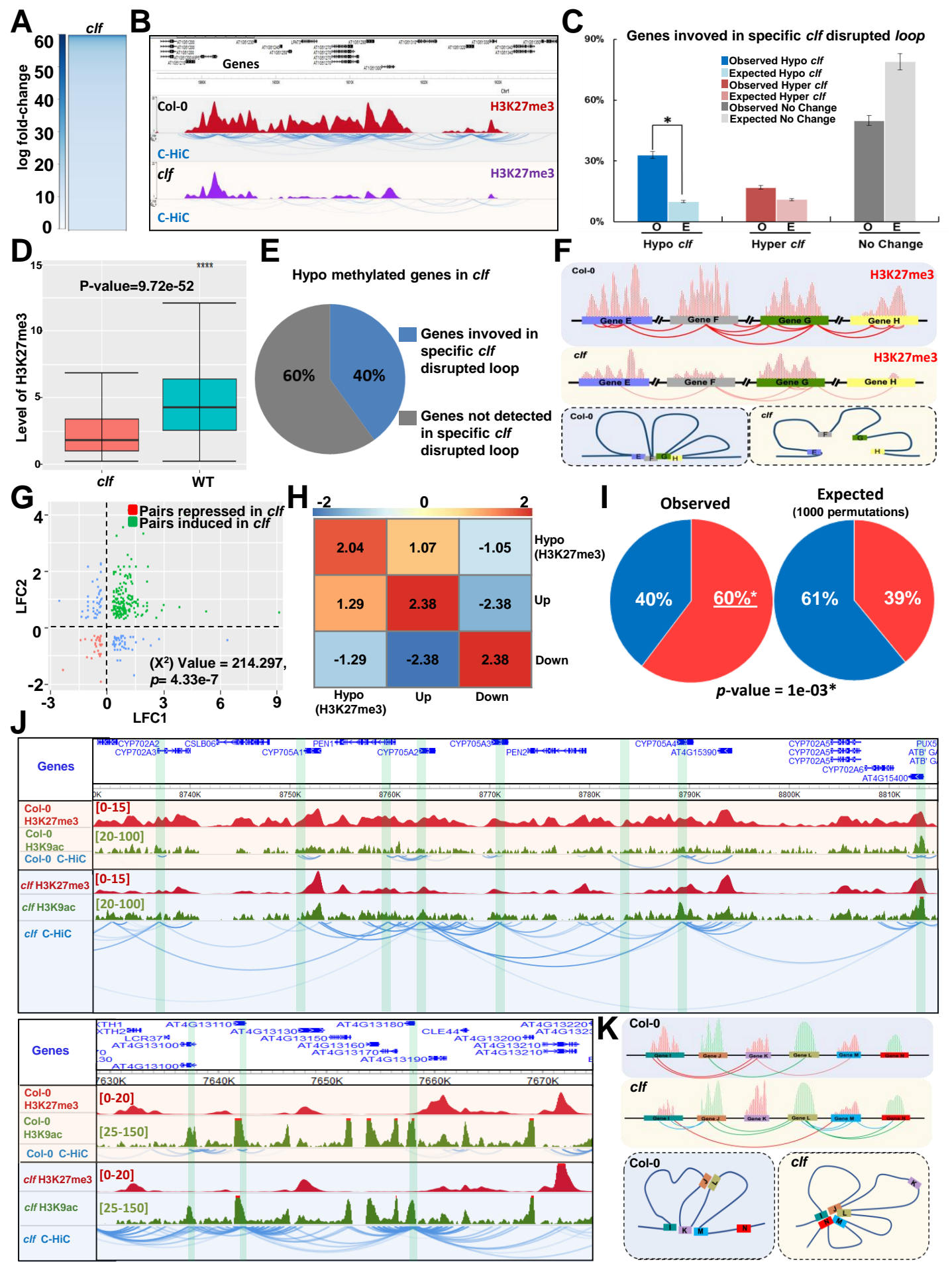
A**B****C****D****E**

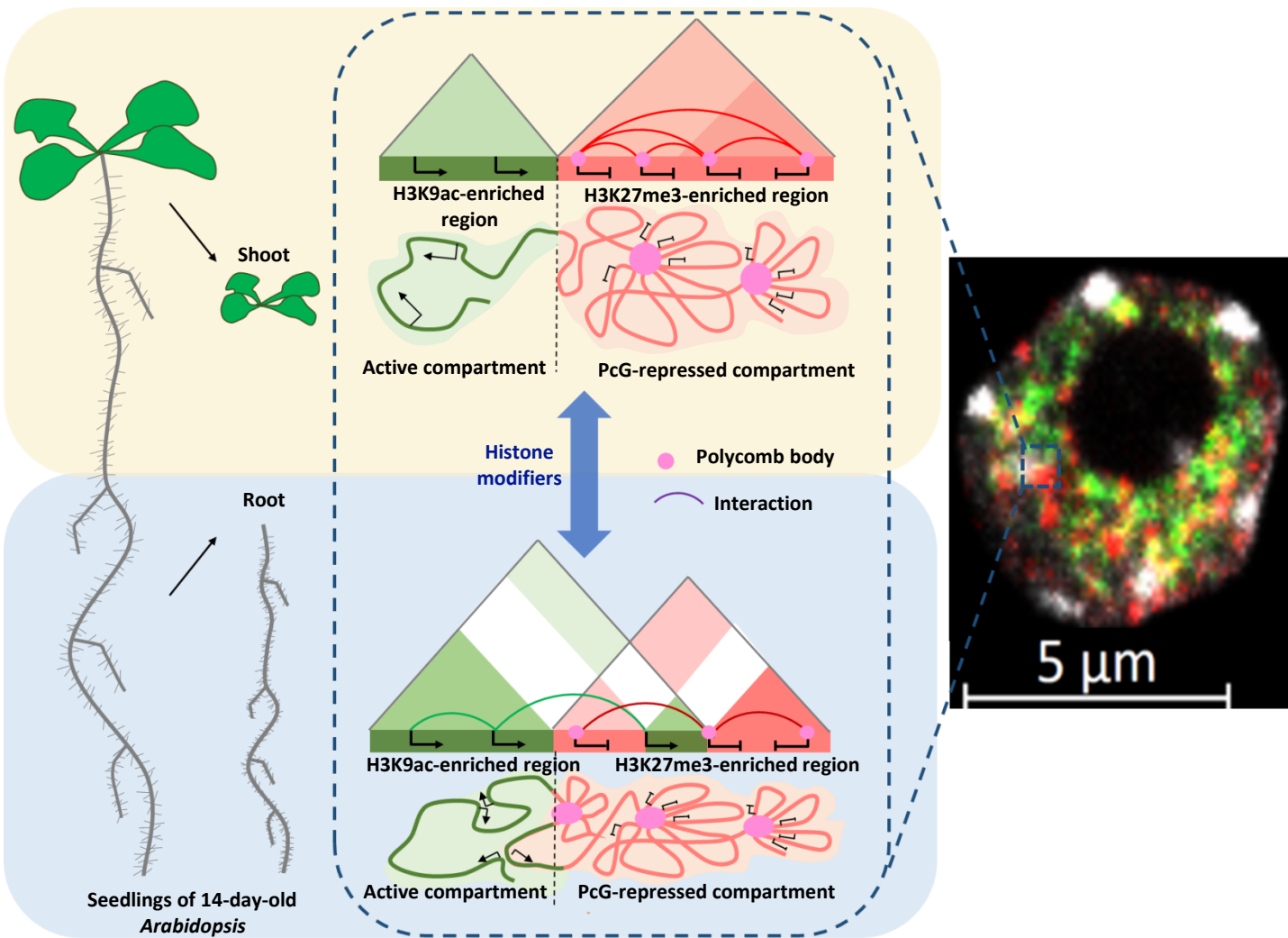




A**B****C****D****E****F**Hyper methylated genes in *ref6-5*

- Red: Genes involved in specific *ref6-5* loops
- Grey: Genes not detected in specific *ref6-5* loops





1 **Supplemental Figure legends**

2 **Supplemental Fig S1.** Immunofluorescence detection of H3K9ac (green) and H3K27me3 (red) chromatin
3 histone modifications and DAPI staining in isolated *Arabidopsis* nuclei. Three independent nuclei are
4 shown, complementary to Figure 1A.

5 **Supplemental Fig S2.** Schematic representation of the HiChIP method.

6 **Supplemental Fig S3.** PCA (principal component analysis) plot for different replicates of HiChIP-shoot and
7 root of wild-type *Arabidopsis*. High reproducibility is observed between the replicates in HiChIP
8 experiments.

9 **Supplemental Fig S4.** Plots representing the H3K9ac (A) and H3K27me3 (B) chromatin loop size
10 distribution.

11 **Supplemental Fig S5.** Visualization of the interaction matrix of HiChIP in shoot and root of wild-type in
12 *Arabidopsis* Chromosome 3. An example of H3K27me3 HiChIP loops showing stronger interactions in
13 shoot compared to root (SSRLs). A shoot loop showing higher signal of H3K27me3 in shoot than root is
14 indicated in the map. ChIP-seq signals of H3K27me3 in shoot and root are shown as blue peaks.

15 **Supplemental Fig S6.** Visualization of the interaction matrix of HiChIP in shoot and root of wide-type in
16 *Arabidopsis* Chromosome 3. An example of H3K27me3 HiChIP loops showing stronger interactions in
17 root than in shoot. A root loop showing higher signal of H3K27me3 in root than shoot is indicated in the
18 map. ChIP-seq signals of H3K27me3 in shoot and root are shown as blue peaks.

19 **Supplemental Fig S7.** Gene pairs connected in shoot specific repressive loops (SSRL) and root specific
20 repressive loops (RSRL) in *Arabidopsis* wide-type. A higher number of gene pairs are repressed in SSRLs
21 than expected randomly (p-value: 4E-175). For RSRLs, a higher number of gene pairs are induced (log FC
22 shoot/root) than expected randomly (p-value: 3.2E-55).

23 **Supplemental Fig S8.** Schematic representation of the Capture Hi-C (C-Hi-C) method.

24 **Supplemental Fig S9.** PCA (principal component analysis) plot for different replicates of Capture Hi-C in
25 *Arabidopsis* wild-type shoot and root. High reproducibility was observed between the replicates in
26 Capture Hi-C experiments.

27 **Supplemental Fig S10.** (A) Pie chart representing the observed and expected proportion of repressed
28 genes in shoot (blue), repressed genes in root (red) and unchanged (grey) among the genes involved in
29 loops detected both with HiChIP and C-Hi-C. (B) Pie chart representing the observed and expected
30 proportion of repressed genes in shoot (blue), repressed genes in root (red) and unchanged (grey,
31 among the genes involved in loops detected both with HiChIP and C-Hi-C. To obtain the expected
32 proportion, we shuffled the gene expression value 1000 times to obtain the randomized gene counts.
33 The mean of the 1000 permutations was used to determine the expected proportions.

34 **Supplemental Fig S11.** PCA (principal component analysis) plots for different replicates of Capture Hi-C
35 experiments of *ref6-5* mutant and wild-type shoot in *Arabidopsis*. A high reproducibility was observed
36 between the replicates in Capture Hi-C experiments.

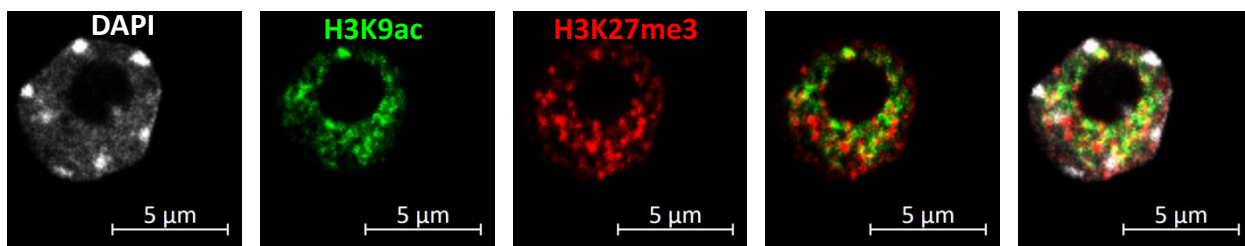
37 **Supplemental Fig S12.** Gene pairs connected in *ref6-5* specific loops (reSL) in *ref6-5* mutant compared to
38 wild-type shoot in *Arabidopsis*. A higher number of gene pairs are repressed in reSLs than expected by
39 chance (p-value = 4E-10).

40 **Supplemental Fig S13.** PCA (principal component analysis) plot for different replicates of *clf* mutant and
41 *Arabidopsis* wild-type. A high reproducibility was observed between the replicates in Capture Hi-C
42 experiments.

43 **Supplemental Fig S14.** Gene pairs connected in *clf* destabilized loops in *clf* mutant. A higher number of
44 gene pairs are induced than expected randomly (p-value: 4.33E-7).

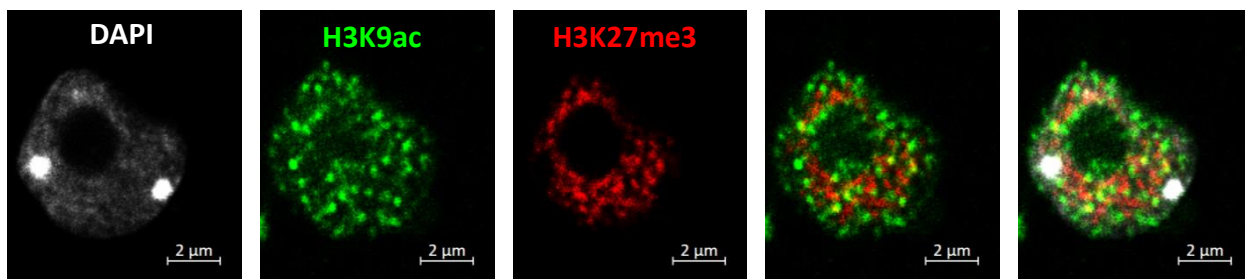
45 **Supplemental Fig S15.** Examples of important developmental genes *AGAMOUS* (*AG*), *AGL24*, *WRKY14*
46 and *CYCB1;5* losing H3K27me3 in *clf* and that tend to establish interactions with regions marked with

47 H3K9ac euchromatin mark. C-Hi-C interactions (blue lines), H3K9ac ChIP-seq signal in wild-type and *clf*
48 (green peaks), H3K27me3 ChIP-seq signal in wild-type and *clf* (red peaks) are represented, respectively.
49 **Supplemental Fig S16.** Hypomethylated gene pairs interacting in *clf* are associated with H3K9ac. A
50 density plot shows that interacting gene pairs in *clf*, which are hypomethylated, are also associated with
51 the active histone modification H3K9ac in wild-type *Arabidopsis*. The frequency of observed Hypo-
52 H3K27me3 and H3K9ac interactions is 60% and is greater than the expected frequency over 1000
53 permutations (39%).



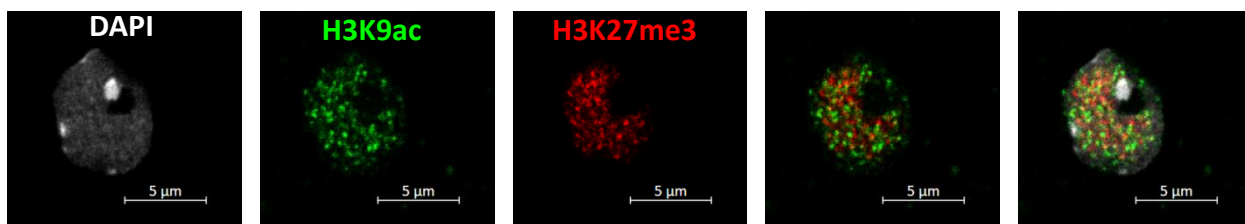
Alexa 488nM

Alexa 555nM



Alexa 555nM

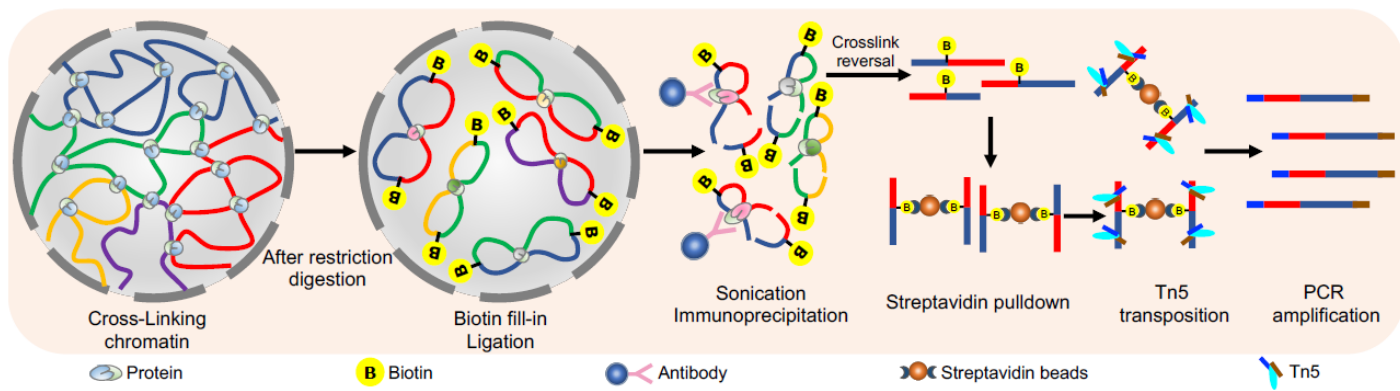
Alexa 488nM



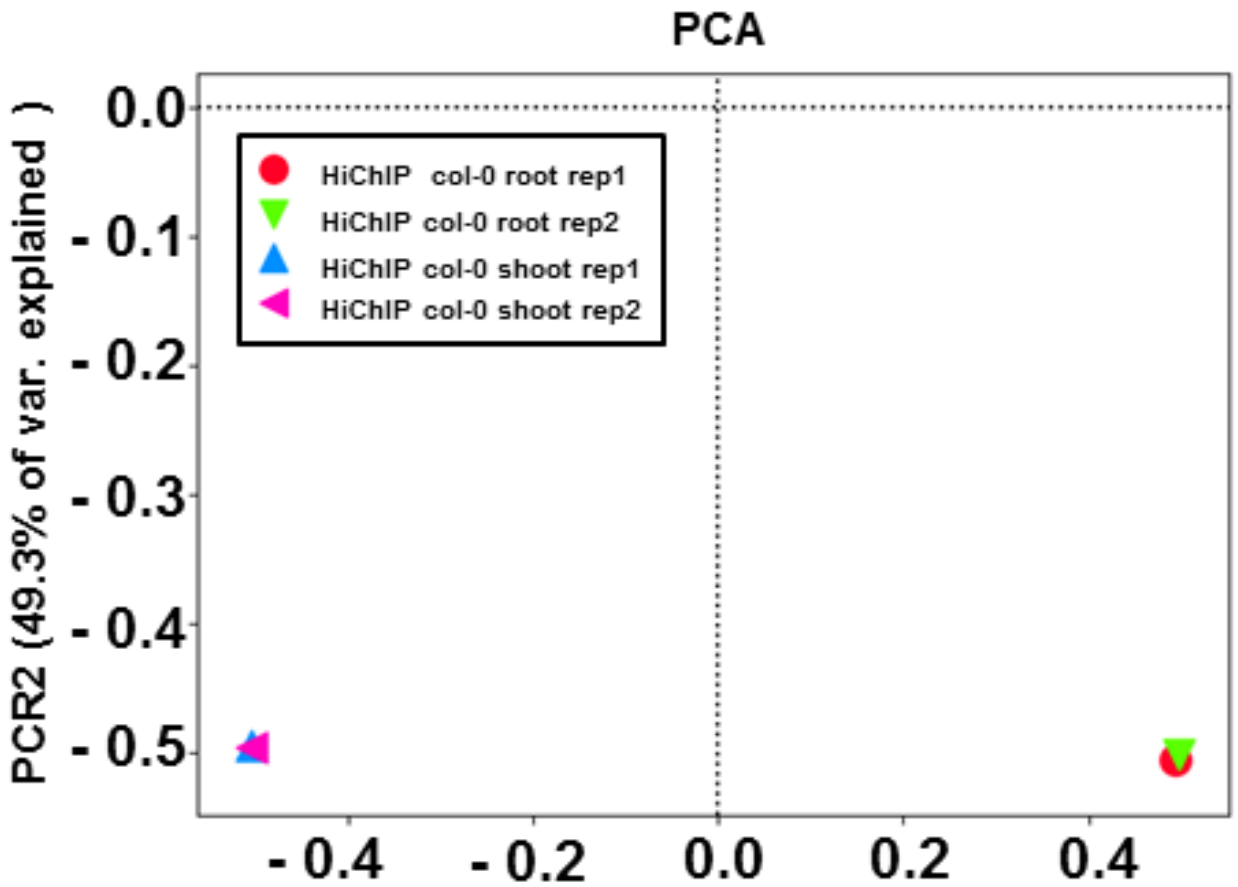
Alexa 555nM

Alexa 488nM

Supplemental Fig S1. Immunofluorescence detection of H3K9ac (green) and H3K27me3 (red) chromatin marks and DAPI staining in isolated *Arabidopsis* nuclei. Three independent nuclei are shown, complementary to Figure 1A.

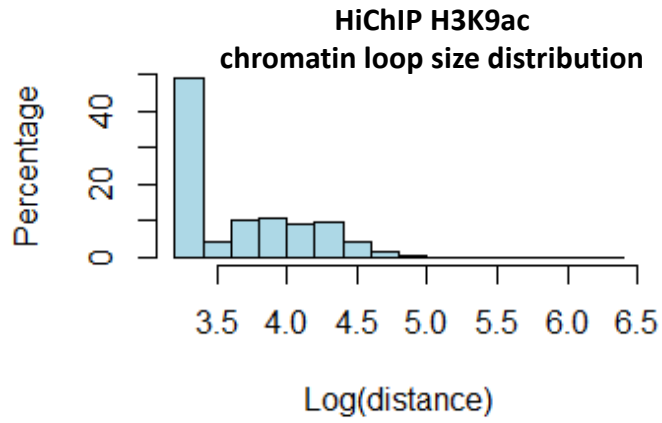


Supplemental Fig S2. Schematic representation of the HiChIP method.

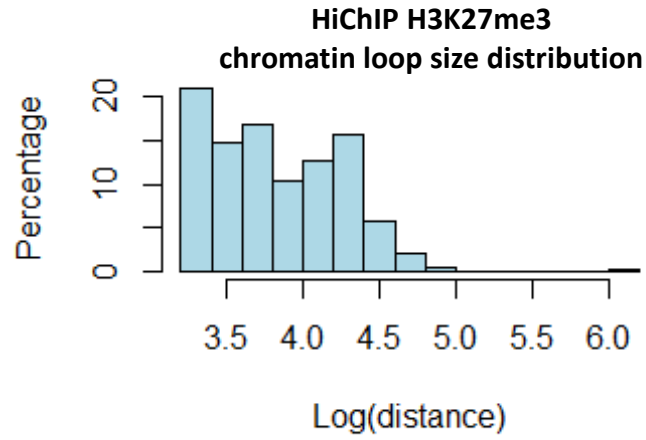


Supplemental Fig S3. PCA (principal component analysis) plot for different replicates of HiChIP-shoot and root of wild-type *Arabidopsis*. High reproducibility is observed between the replicates in HiChIP experiments.

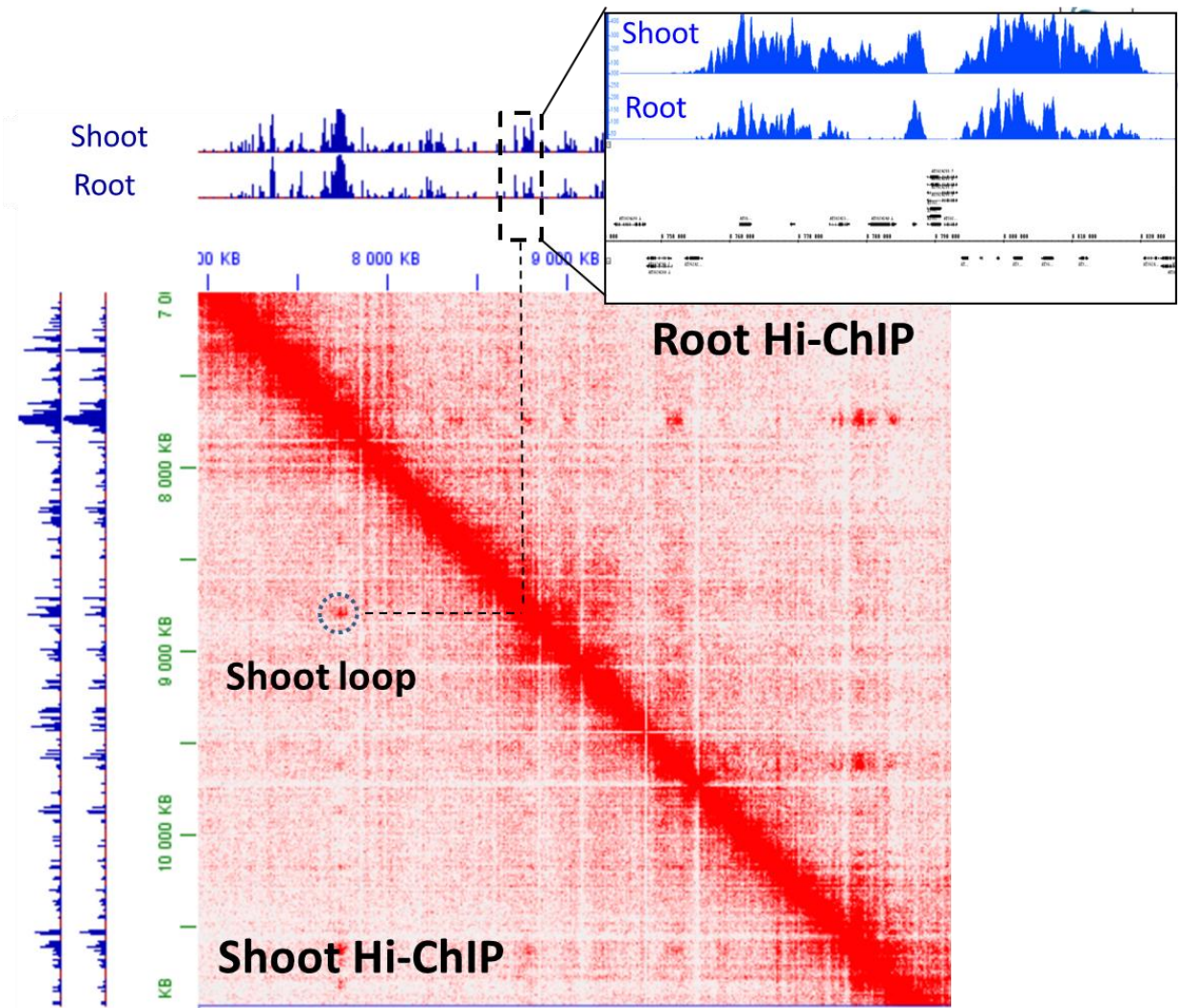
A



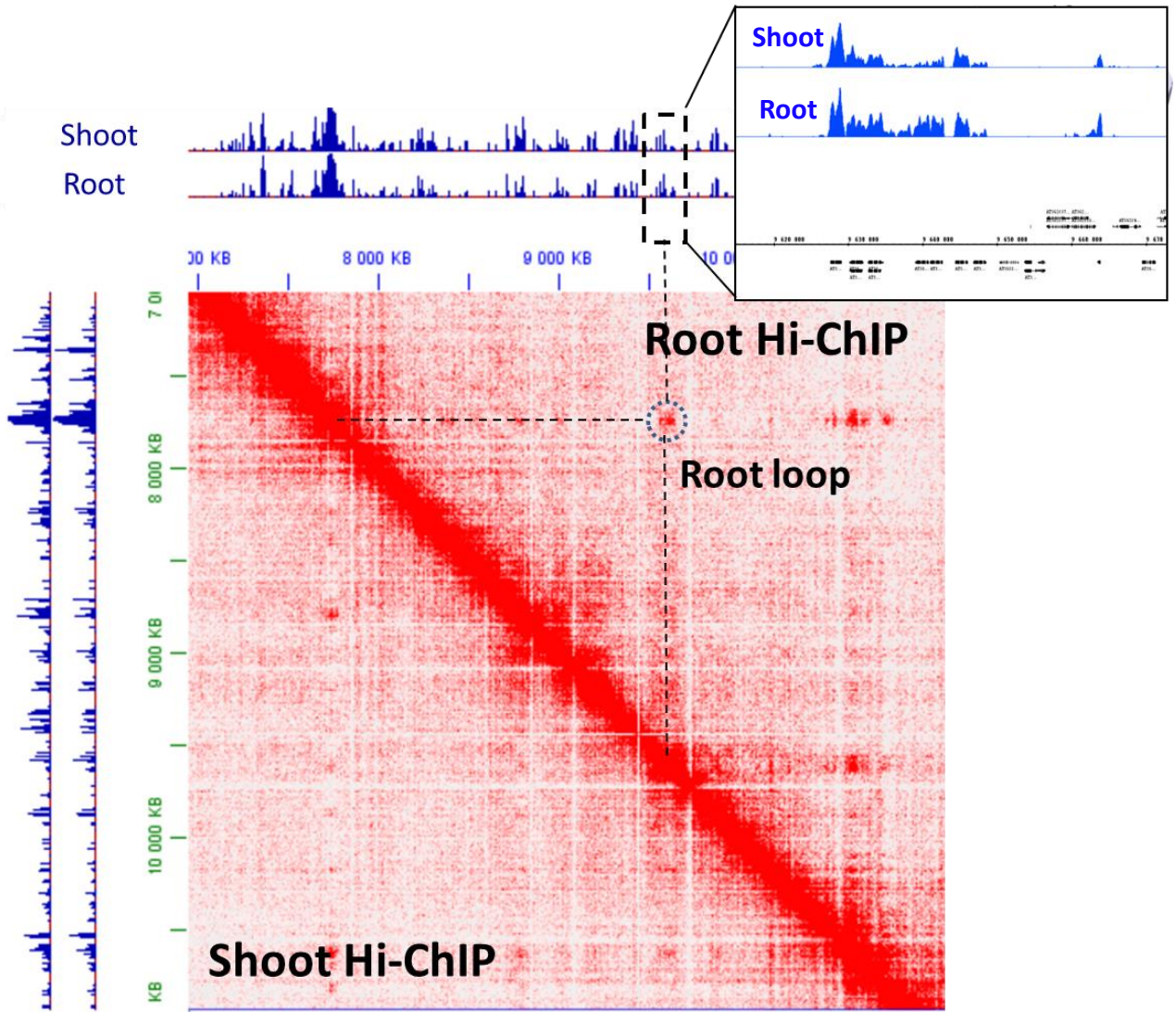
B



Supplemental Fig S4. Plots representing the H3K9ac (**A**) and H3K27me3 (**B**) chromatin loop size distribution



Supplemental Fig S5. Visualization of the interaction matrix of HiChIP in shoot and root of wild-type in *Arabidopsis* Chromosome 3 . An example of H3K27me3 HiChIP loops showing stronger interactions in shoot compared to root (SSRLs). A shoot loop showing higher signal of H3K27me3 in shoot than root is indicated in the map. ChIP-seq signals of H3K27me3 in shoot and root are shown as blue peaks.



Supplemental Fig S6. Visualization of the interaction matrix of HiChIP in shoot and root of wide-type in *Arabidopsis* Chromosome 3. An example of H3K27me3 HiChIP loops showing stronger interactions in root than in shoot. A root loop showing higher signal of H3K27me3 in root than shoot is indicated in the map. ChIP-seq signals of H3K27me3 in shoot and root are shown as blue peaks.

A

Shoot specific repressive loops (SSRL)	Gene1-Log FC >0 induced	Gene1-Log FC_1<0 repressed
Gene2-Log FC >0 induced	194	362
Gene2-Log FC_1<0 repressed	411	1033*

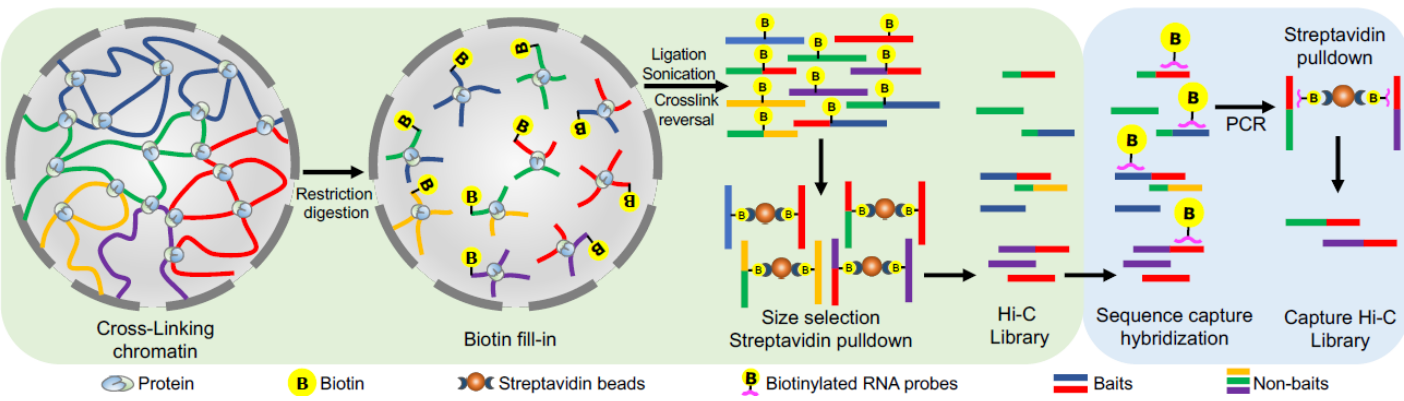
$\chi^2 (3, N = 2000) = 809.38, p = 4.0E-175$

B

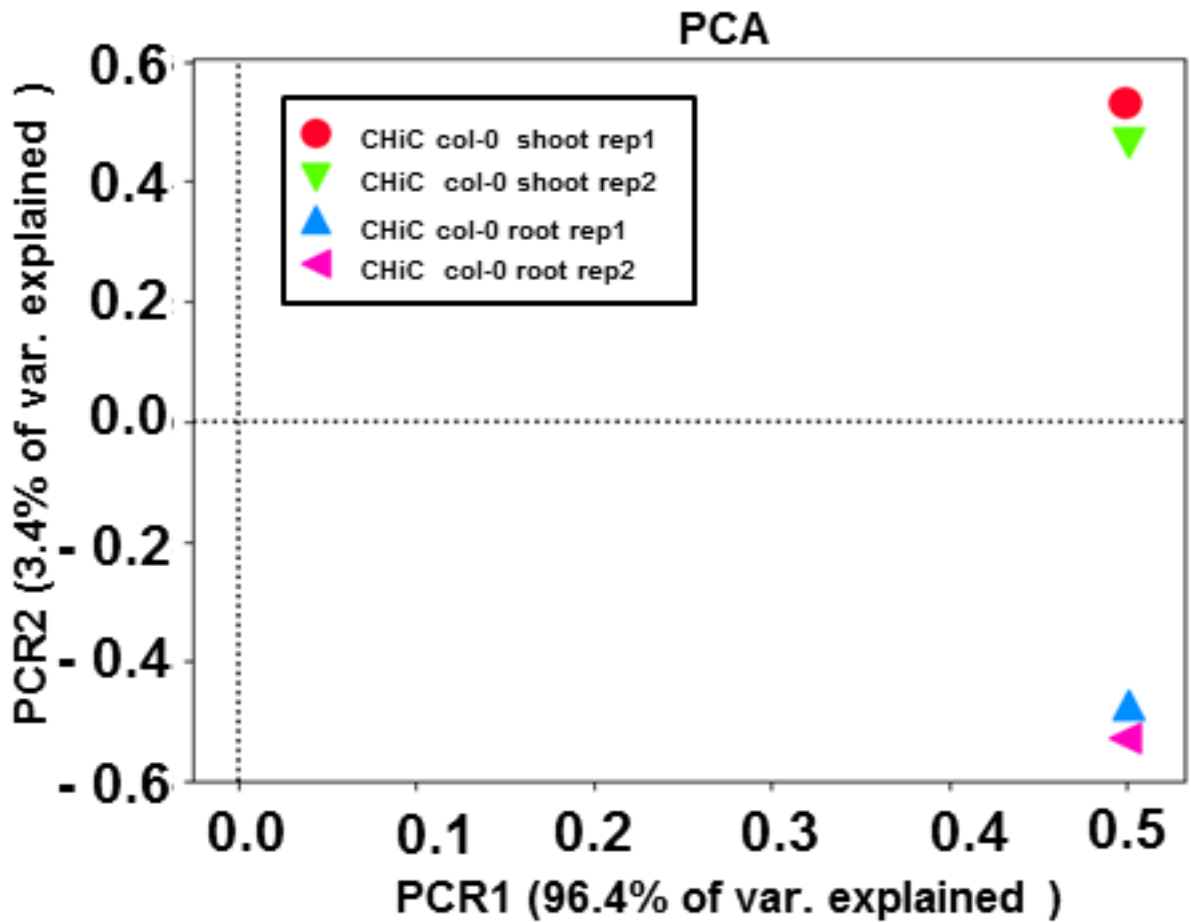
Root specific repressive loops (RSRL)	Gene1-Log FC >0 induced	Gene1-Log FC_1<0 repressed
Gene2-Log FC >0 induced	801*	443
Gene2-Log FC_1<0 repressed	425	331

$\chi^2 (3, N = 2000) = 256.072, p=3.2E-55$

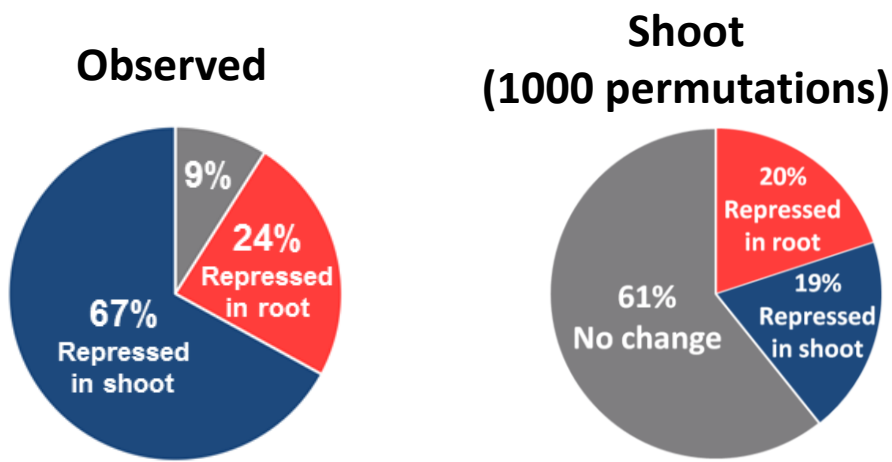
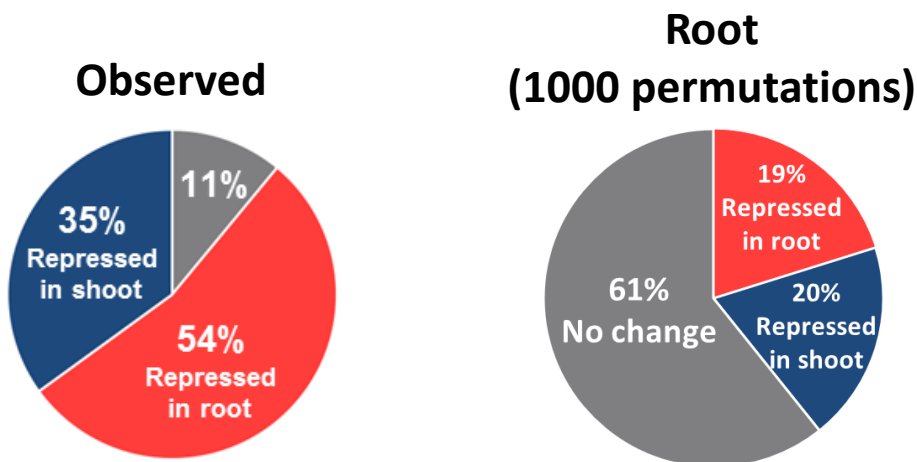
Supplemental Fig S7. Gene pairs connected in shoot specific repressive loops (SSRL) and root specific repressive loops (RSRL) in *Arabidopsis* wide-type. A higher number of gene pairs are repressed in SSRLs than expected randomly (p-value: 4E-175). For RSRLs, a higher number of gene pairs are induced (log FC shoot/root) than expected randomly (p-value: 3.2E-55).



Supplemental Fig S8. Schematic representation of the Capture Hi-C (C-Hi-C) method.

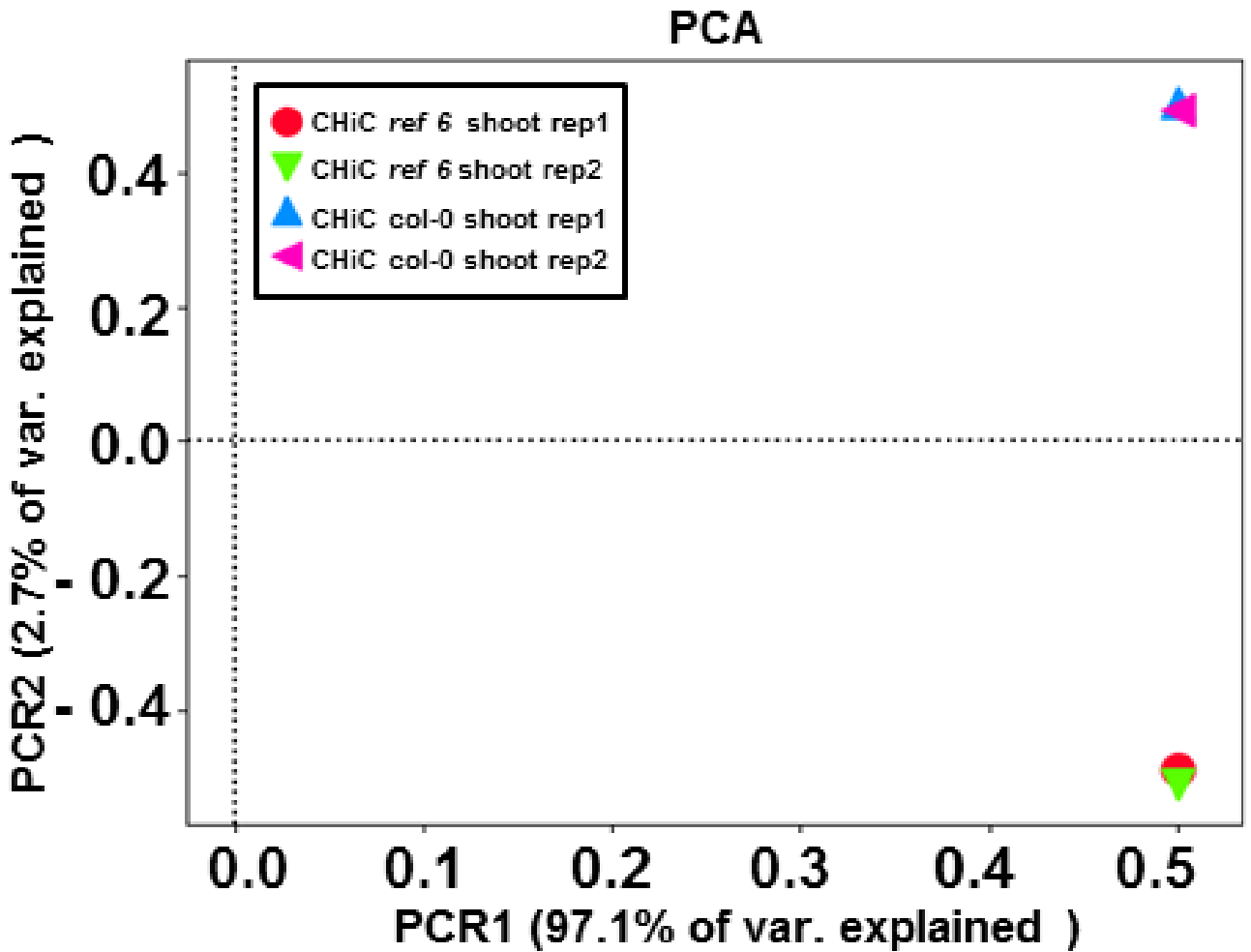


Supplemental Fig S9. PCA (principal component analysis) plot for different replicates of Capture Hi-C in *Arabidopsis* wild-type shoot and root. High reproducibility was observed between the replicates in Capture Hi-C experiments.

A**B**

Supplemental Fig S10. (A) Pie chart representing the observed and expected proportion of repressed genes in shoot (blue), repressed genes in root (red) and unchanged (grey) among the genes involved in loops detected both with HiChIP and C-Hi-C. **(B)** Pie chart representing the observed and expected proportion of repressed genes in shoot (blue), repressed genes in root (red) and unchanged (grey,) among the genes involved in loops detected both with HiChIP and C-Hi-C.

To obtain the expected proportion, we shuffled the gene expression signals 1000 times to obtain a randomized one. The mean of the 1000 permutations was used to determine the expected proportions.

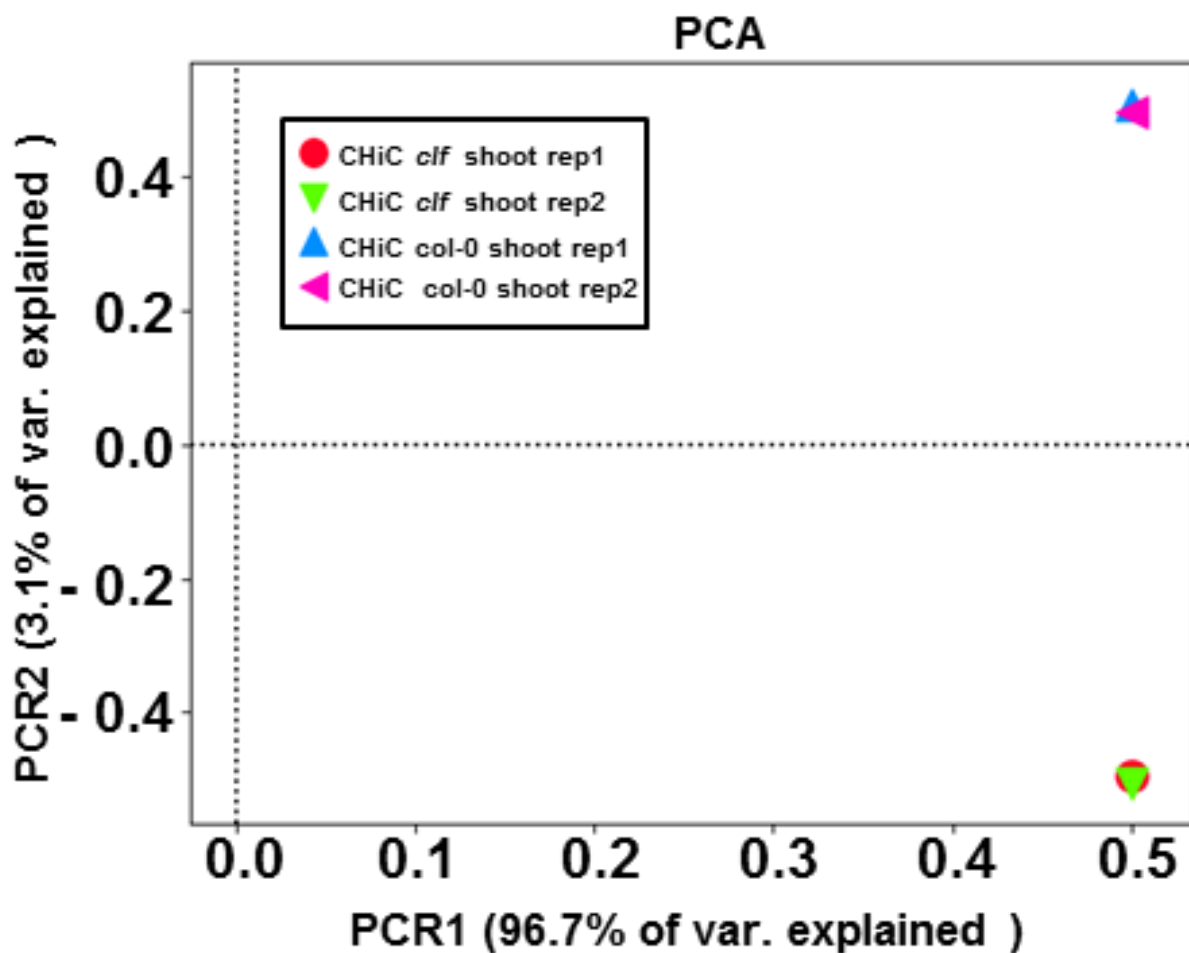


Supplemental Fig S11. PCA (principal component analysis) plots for different replicates of Capture Hi-C experiments of *ref6-5* mutant and wild-type shoot in *Arabidopsis*. A high reproducibility was observed between the replicates in Capture Hi-C experiments.

Interactions gained in <i>ref6-5</i>	Gene1-Log FC >0 induced	Gene1-Log FC_1<0 repressed
Gene2-Log FC >0 induced	117	116
Gene2-Log FC_1<0 repressed	113	200*

$$X^2 (3, N = 2000) = 39.1, p = 4E-10$$

Supplemental Fig S12. Gene pairs connected in *ref6-5* specific loops (reSL) in *ref6-5* mutant compared to wild-type shoot in *Arabidopsis*. A higher number of gene pairs are repressed in reSLs than expected by chance (p-value = 4E-10).

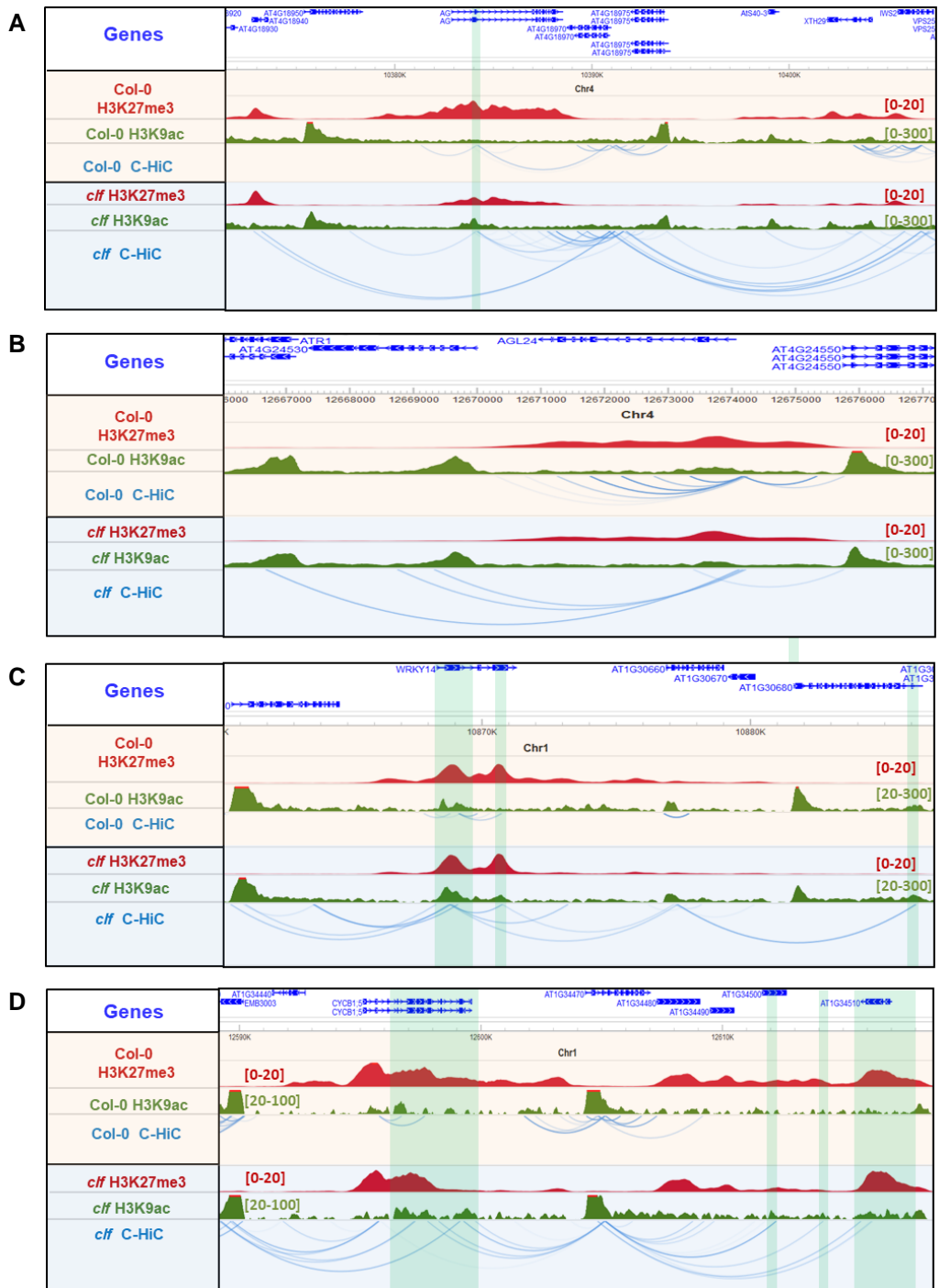


Supplemental Fig S13. PCA (principal component analysis) plot for different replicates of *clf* mutant and *Arabidopsis* wild-type. A high reproducibility was observed between the replicates in Capture Hi-C experiments.

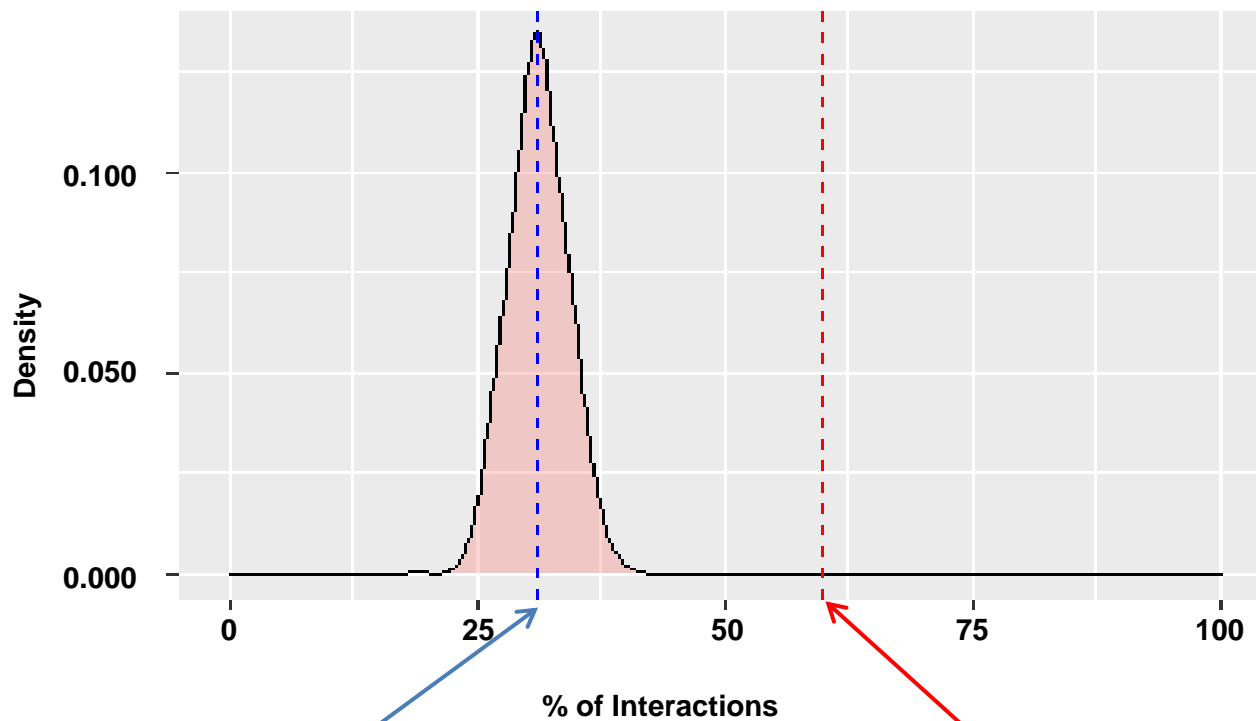
Interactions lost in <i>clf</i>	Gene1-Log FC >0 induced	Gene1-Log FC_1<0 repressed
Gene2-Log FC >0 induced	185*	43
Gene2-Log FC_1<0 repressed	43	30

$$\chi^2 (3, N = 2000) = 214.297, p = 4.33E-7$$

Supplemental Fig S14. Gene pairs connected in *clf* destabilized loops in *clf* mutant. A higher number of gene pairs are induced than expected randomly (p-value: 4.33E-7).



Supplemental Fig S15. Examples of important developmental genes AGAMOUS (AG), AGL24, WRKY14 and CYCB1;5 losing H3K27me3 in *clf* and that tend to establish interactions with regions marked with H3K9ac euchromatin mark. C-Hi-C interactions (blue lines), H3K9ac ChIP-seq signal in wild-type and *clf* (green peaks), H3K27me3 ChIP-seq signal in wild-type and *clf* (red peaks) are represented, respectively.



Expected
Hypo-H3k27me3 and H3K9ac = 39%

Observed
Hypo-H3k27me3 and H3K9ac = 60%

Supplemental Fig S16. Hypomethylated gene pairs interacting in *clf* are associated with H3K9ac. A density plot shows that interacting gene pairs in *clf*, which are hypomethylated, are also associated with the active mark H3K9ac in wild-type *Arabidopsis*. The frequency of observed Hypo-H3K27me3 and H3K9ac interactions is 60% and is greater than the expected frequency over 1000 permutations (39%).